

Predicting the dynamic moduli and viscosities of bitumens via oscillatory strain-controlled molecular simulations

Assaf, Eli I.; Liu, Xueyan; Erkens, Sandra

DOI

[10.1016/j.molliq.2024.126637](https://doi.org/10.1016/j.molliq.2024.126637)

Publication date

2024

Document Version

Final published version

Published in

Journal of Molecular Liquids

Citation (APA)

Assaf, E. I., Liu, X., & Erkens, S. (2024). Predicting the dynamic moduli and viscosities of bitumens via oscillatory strain-controlled molecular simulations. *Journal of Molecular Liquids*, 418, Article 126637. <https://doi.org/10.1016/j.molliq.2024.126637>

Important note

To cite this publication, please use the final published version (if applicable). Please check the document version above.

Copyright

Other than for strictly personal use, it is not permitted to download, forward or distribute the text or part of it, without the consent of the author(s) and/or copyright holder(s), unless the work is under an open content license such as Creative Commons.

Takedown policy

Please contact us and provide details if you believe this document breaches copyrights. We will remove access to the work immediately and investigate your claim.



Predicting the dynamic moduli and viscosities of bitumens via oscillatory strain-controlled molecular simulations

Eli I. Assaf^{a,*}, Xueyan Liu^a, Sandra Erkens^{a,b}

^a Delft University of Technology, Delft, The Netherlands

^b Ministry of Infrastructure and Water Management (Rijkswaterstaat), The Netherlands

ARTICLE INFO

Keywords:

Molecular dynamics
Dynamic properties
Viscoelasticity
Rheology

ABSTRACT

This study employs strain-controlled oscillatory deformations in Molecular Dynamics (MD) simulations to evaluate the dynamic properties of all-atom molecular systems, specifically targeting the SARA fractions of bitumen. Twelve molecular systems representing these fractions were modeled using the PCFF force field. The simulations effectively captured their viscoelastic properties across multiple frequency domains, including Elastic, Glassy, Rubbery, and Viscous responses. Reported storage and loss moduli range from thousands to tens of megapascals, with viscosities from tens to near-zero Pascal-seconds across various frequencies and temperatures, aligning well with experimental observations. Saturates and Aromatics were identified as the softest and most thermally susceptible fractions, while Resins and Asphaltenes were the stiffest and least susceptible. The study reveals that the relaxation time of all-atom molecular systems is significantly shorter than in experimental setups, necessitating careful comparison of stress-related phenomena across equivalent relaxation times. Although this allows for the exploration of response profiles in computationally tractable simulations, the nature of all-atom force fields and simulation algorithms introduces spatiotemporal scale discrepancies that must be addressed in future simulations involving the study of stress-related phenomena using MD.

1. Introduction

Bitumen—a complex blend of high molecular weight hydrocarbons—is primarily obtained from the fractional distillation of petroleum in the lower sections of distillation columns. With an annual production exceeding 100 million tons, bitumen holds substantial industrial importance, particularly in the oil, gas, and construction sectors. Contemporary research focuses on developing more sustainable and durable forms of bitumen and heavy oils that remain workable at lower temperatures. While experimental studies have historically dominated bitumen research, the need for fundamental characterization and design techniques has driven a shift toward molecular simulation methods.

At the molecular level, bitumen comprises a diverse assortment of hydrocarbons, typically classified as oily, resinous, or asphaltenic compounds [1]. These constituents confer unique viscoelastic properties to bitumen, which are critical for its mechanical performance in construction applications but also complicate its mechanical and rheological characterization. Unlike materials that are purely viscous or purely elastic, bitumen exhibits a stress response dependent on the strain rate within its operational conditions. This strain rate dependency introduces

variability in its mechanical characteristics, both experimentally and computationally [2].

Dynamic Mechanical Analysis (DMA) is a standard experimental technique used to measure the mechanical response of viscoelastic materials like bitumen [3]. In DMA, a sample is subjected to an oscillatory shear strain, typically in a sinusoidal pattern, and the resulting stress is recorded along with the phase lag (δ) between the strain and stress [4]. This phase lag and the stress amplitude are used to characterize the material's behavior at specific strain rates and to construct master curves that describe the response across a range of strain rates and temperatures [5]. DMA forms the foundation for many research efforts aiming to characterize the performance of viscoelastic compounds.

In computational studies, modeling the dynamic properties of viscoelastic materials is less common, largely due to challenges in defining, handling, and interpreting stresses in Molecular Dynamics (MD) simulations. Stress, defined as potential energy per unit volume, is ambiguous on a per-atom basis because atoms lack a clearly defined volume [6]. Additionally, atomistic force fields, which govern atomic motion in simulations, involve numerous interaction terms—such as van

* Corresponding author.

E-mail address: e.i.assaf@tudelft.nl (E.I. Assaf).

<https://doi.org/10.1016/j.molliq.2024.126637>

Received 9 August 2024; Received in revised form 15 November 2024; Accepted 28 November 2024

Available online 12 December 2024

0167-7322/© 2024 The Author(s). Published by Elsevier B.V. This is an open access article under the CC BY license (<http://creativecommons.org/licenses/by/4.0/>).

der Waals forces, bonds, and angles—to model molecular dynamics. These force fields generate instantaneous stress values that include contributions from intramolecular strains, such as bond and angle bending, which may not correspond to observable stresses in large-scale material tests. Consequently, MD simulation scripts require careful adjustments to mitigate numerical artifacts and atomistic interactions that, while essential for simulating atomic motion, do not manifest in large-scale mechanical properties but can significantly affect stress measurements.

Moreover, the time-dependent nature of stress-dependent properties further complicates computational analysis. Generally, a stress response arises as a reaction to an applied perturbation, reflecting Newton's third law. The response is therefore influenced by the characteristic timescale of the perturbation, meaning that any material may exhibit fluid-like or solid-like responses depending on how fast or slow the perturbation is relative to the material's internal dynamics [7]. This is particularly evident in viscoelastic materials, where both viscous and elastic responses are significant under stress perturbations experienced in practical applications. Such observations can heavily affect the comparison of experimentally and computationally obtained stress values generated under seemingly "equal" or "equivalent" setups possessing inherently different characteristic times [8].

Despite the comprehensiveness of force field equations in mimicking the intricate nature of molecular interactions, their inherent simplification of complex molecular motions imparts atoms and molecules with an inherently higher number of degrees of freedom [9,10]. This translates into considerably faster material dynamics, necessitating faster or larger perturbations in simulations to elicit the same response as observed under experimental conditions. Such spatiotemporal discrepancies are not new to the field of force field dynamics. While force fields—whether highly detailed all-atom or simplified coarse-grained models—often utilize artificial constraints to force-fit certain material properties (e.g., density, heat capacity, heat of vaporization), seldom, if ever, have force fields been developed to explicitly fit stress-related phenomena as observed in DMA tests [11,12]. As a result, the characteristic times derived from stress-induced perturbations in molecular simulations involving conventionally used force fields may not scale correctly with experimental observations, even when unit consistency and seemingly equivalent setups are utilized [13].

Multiple simulation frameworks and techniques have been devised to capture relevant mechanical and rheological properties. However, these often include simplifications that make them material-specific and reduce their applicability or transferability to the study of other materials, especially those that are viscoelastic. This scarcity of DMA-like simulation frameworks and standards is seldom addressed by researchers specialized in computational chemistry and molecular dynamics [14,15]. For example, Green-Kubo methods aim to obtain stress-related properties by utilizing autocorrelation functions to estimate the average values of stress tensors in simulations not subject to any external perturbations, thus providing insight into the material's behavior under very low or near-zero shear stress conditions [16]. These techniques depend on the fact that molecular systems' instantaneous properties vary, even though they tend toward a well-defined average at equilibrium. By capturing small variations in stress tensors and volume deformations, researchers can obtain stress measurements. These autocorrelation methods work well with low-viscosity Newtonian fluids but prove insufficient in capturing the response of materials with a more complex mechanical response [7,17]. Moreover, such materials are also affected by numerical (artificial) and intramolecular intricacies present in highly complex hydrocarbons, preventing the autocorrelation functions from converging within MD-tractable times and the application of such methods altogether to such materials [18,19]. Moreover, obtaining zero-shear quantities like zero-shear viscosity may provide some insights into the material's mechanical nature but does not fundamentally describe its mechanical response as obtained using DMA analysis. A stress-induced perturbation, even if simplistic, is needed to effectively

quantify the material's mechanical or rheological response [3].

Researchers like Greenfield [20] have devised methods to compute dynamic properties based on the available degrees of freedom, especially those that describe intramolecular conformations, to characterize the viscoelastic nature of the material. While computationally efficient and promising, the nature of these methodologies deviates considerably from those used in the laboratory, making interpretation of the observations challenging, especially when compared to observations made using a DMA-like background.

More elaborate methods have been developed to explicitly introduce the impact of external shearing fields, such as those by Müller-Plathe [21], Zhao [22], Hess [23]. These non-equilibrium methods aim to introduce stress-induced perturbations to the system of molecules at controlled amplitudes and rates, study how the material reacts to these perturbations, and determine how long it takes to adapt to the applied strain. This approach produces a more meaningful set of quantities that better describe how the material responds to perturbations similar to those applied during DMA tests. While closer in principle to the nature of experimental DMA tests, the nature of the perturbations and simulation setups does not precisely mimic the phenomena in DMA tests, again adding setup-to-setup discrepancies that make their use challenging when comparing to experimentally obtained DMA results. Moreover, such methods have been successfully applied in studies involving only low-viscosity Newtonian fluids [19] – not on highly viscoelastic compounds – and little attention is given to accounting for the ratio of fundamentally different characteristic times that describe seemingly equal setups experimentally and/or computationally.

This oversight is particularly pronounced in the study of bitumen, where the computation of viscosity and other dynamic properties using MD simulations is notably limited. Research involving bitumen is predominantly application-driven and rooted in civil engineering disciplines, focusing on practical performance metrics rather than molecular-level understanding. Consequently, computational chemistry approaches to modeling bitumen are less developed, leading to a scarcity of specialized simulation methods tailored for such materials. As a result of these challenges, numerous research articles report overestimated stress-related properties—such as stress tensors in the gigapascal range when experimentally they should be within the megapascal range—and underestimated viscosity values, like those in the millipascal-second range when they are experimentally in the pascal-second range [24]. These discrepancies can often be attributed to the omission of accounting for the fundamentally different characteristic timescales between differing setups, whether between experimental and computational configurations or even among distinct computational setups.

In this manuscript, we aim to compute the dynamic properties of bituminous materials by carefully mimicking the principles of DMA tests through the application of strain-controlled oscillatory deformations using all-atom MD simulations. Our objective is to capture relevant rheological properties by conducting comprehensive frequency and temperature-dependent sweep tests across various hydrocarbon blends. This approach seeks to overcome the aforementioned challenges and enhance the use of MD simulations in exploring the rheological response of materials, advancing the characterization and design of bitumens using molecular methods. This manuscript also aims to integrate concepts from Rheology and Civil Engineering into Computational Chemistry, establishing a standardized simulation framework interpretable and applicable across multiple disciplines. Additionally, by offering a clearer understanding of how the characteristic times of observed phenomena may influence the results, we aim to enhance the conduct, reporting, and validation of molecular simulations. This will ensure that future iterations of projects involving observed phenomena are more effectively compared to others with similar, but not identical, simulation and/or experimental setups (e.g., between simulations setups using different force fields whose characteristic times may be similar, but not identical).

The manuscript begins with the [Section 2](#), which outlines the selection of molecules used to represent the SARA (Saturated, Aromatic, Resinous, and Asphaltenic) fractions in bitumen, the choice of the force field, and the steps required to prepare the molecular systems for use during testing. The [Section 3](#) provides a detailed description of the assumptions and parameters used to perform oscillatory deformations using MD, including the definition of the simulation box, the strain waveform used, stress definition in an MD setup, stress measurement and extraction, and the dynamic properties analyzed. The [Section 4](#) details the LAMMPS routines used to mimic DMA tests while efficiently obtaining these properties. The [Section 5](#) summarizes the thermophysical and dynamic properties reported in this study. The manuscript then presents the findings in the [Section 6](#), followed by an in-depth analysis in the [Section 7](#). Finally, it concludes with a summary of the key findings, including relevant dynamic properties, as well as the limitations, challenges, and potential solutions to the methods applied in this study.

2. Molecular models

2.1. Molecules selection

The molecular ensemble in this study consists of 12 molecules, based on the work of Shisong et al [25]. This set is based on the original 12 molecules proposed by Greenfield et al. [20], incorporating structural modifications to align with the SARA (Saturates, Aromatics, Resins, and Asphaltenes) fractionation and functional analysis of bitumen samples from three different sources.

This collection aims to represent a wide range of hydrocarbon classes typically found in bituminous materials, such as alkanes, alkenes, polycyclic aromatics, and non-aromatics, and includes functional groups like phenols, oxanes, pyridines, ketones, thiophenes, and sulfoxides. The molecules selected are generally characterized by high molecular masses, pronounced aromaticity, and significant planarity—traits that are prevalent in bitumens and conducive to studies involving viscoelastic responses.

Moreover, this collection of molecules has been thoroughly assessed to represent SARA fractions in bitumens [26]. This categorization provides a rough estimate of the physical properties expected from each molecule and is such that Saturates are expected to be the most liquid-like, Aromatics and Resins gel-like, and Asphaltenes the most solid-like [27], thus providing a wide array of known physical traits useful

for validation of MD simulations [28]. The molecular details, including their chemical formulas, masses, and estimated densities, are documented in [Table 1](#). Their corresponding SMILES notation can be found in *molecules_selection.docx* in the [Supplementary Information](#).

2.2. Force field selection

The simulations involve all-atom models that employ the Polymer Consistent Force Field (PCFF) [29], with the potential energy of the system (E_{PCFF}) given in Eq. (1). A comprehensive description of the energy contributions for each interaction type is provided in [Table 2](#).

$$E_{PCFF} = \sum E^b + E^{ia} + E^{oa} + E^t + E^{bb} + E^{ba} + E^{bt} + E^{aa} + E^{at} + E^{tt} + E^{VDW} + E^{coul} \quad (1)$$

The PCFF force field is specifically chosen because it is designed to model complex organic mixtures (oily, resinic, or asphaltenic in nature), and has been thoroughly applied to perform simulations of similar all-atom systems involving deformation routines (in size and/or shape). Folder */pcff_parameters* in the [Supplementary Information](#) contains a LAMMPS script containing a model of bitumen encompassing all the force field type and charge parameters used to run all the simulations of this study.

Several all-atom force fields commonly applied in condensed amorphous hydrocarbon mixtures were evaluated, including COMPASS II [31], CHARMM [32], and GAFF2 [33]. Among these, the PCFF force field was selected for its efficacy in modeling the atomic types and interactions specific to the molecular systems under study. More importantly, PCFF includes numerous cross-coupling terms, which limit the system's degrees of freedom—a characteristic particularly suited to this study's simulations, which aim to be highly conservative, adhering as closely as possible to observations expected from first-principle approaches. This conservativeness is intended to reduce spatiotemporal variations across computational configurations, thereby emphasizing discrepancies likely to arise between computational and experimental conditions.

It is worth noting that using an alternative force field or modifying any simulation aspect would necessitate a meticulous comparison of the characteristic times observed in each setup. This approach remains essential for ensuring that the principles discussed here apply consistently, even if, in this study, the comparative setups involve one

Table 1

The chemical structures of molecules employed in this study are depicted herein. Within the Saturates fraction, are (1) Squalane and (2) Hopane. The Aromatics encompass (3) Dioctylcyclohexane naphthalene and (4) Perhydrophenanthrene naphthalene. In the Resins, (5) Quinolinhopane, (6) Thioisorenieratane, (7) Ben-zobisbenzothiophene, (8) Pyridinohopane, and (9) Trimethylbenzeneoxane. Lastly, the Asphaltenes comprises (10) Phenolic, (11) Pyrrolic, and (12) Thiophenic asphaltene.

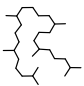
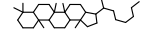
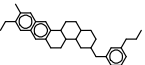
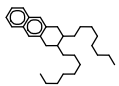
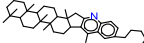
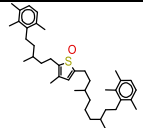
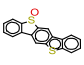
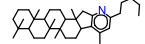
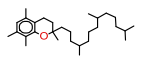
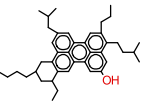
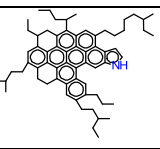
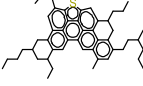
Saturates		Aromatics		Resins	
					
1 C ₃₀ H ₆₂ 422.8 0.803	2 C ₃₈ H ₆₂ 482.9 0.913	3 C ₃₀ H ₄₆ 406.7 0.916	4 C ₃₈ H ₄₄ 464.7 1.030	5 C ₄₀ H ₆₉ N 553.9 1.007	6 C ₄₀ H ₆₀ OS 589.0 1.010
Resins			Asphaltenes		
					
7 C ₁₈ H ₁₀ OS ₂ 306.4 1.540	8 C ₃₈ H ₆₇ N 503.9 0.977	9 C ₂₉ H ₅₀ O 414.7 0.893	10 C ₄₂ H ₅₄ O 574.9 1.049	11 C ₆₀ H ₈₁ N 888.4 1.104	12 C ₅₁ H ₆₂ S 707.1 1.100

Table 2

The PCFF potential energy terms involve symbols i, j, k, l , and m for atom groups, with variables representing interatomic distances (r_{ij}), in-plane angles (θ_{ijk}), out-of-plane angles (χ_{ijk}), and dihedral angles (φ_{ijkl}). Multiplicity (M), force field constants ($k, r^0, \theta^0, \chi^0, \varphi^0, s_0, \epsilon_{ij}$ and ϵ_0), and partial atomic charges (q_i) are also included.

Interaction term	Expression
Bond bending	$E^b = \sum_{ij} \sum_{M=2}^4 k_{(m)ij} (r_{ij} - r_{ij}^0)^m$
In-plane angle bending	$E^{ia} = \sum_{ijk} \sum_{M=2}^4 k_{a,ijk}^m (\theta_{ijk} - \theta_{(m),ijk}^0)^m$
Out-of-plane angle bending	$E^{oa} = \sum_{ijk} k_{ijk} \cdot (\chi_{ijk} - \chi_{ijk}^0)^2$
Symmetric torsional angle bending	$E^t = \sum_{ijkl} \sum_{m=1}^4 k_{(m)ijkl} (1 + \cos(m\varphi_{ijkl} - \varphi_{(m)ijkl}^0))$
Cross-coupling bond-bond	$E^{bb} = \sum_{ijkl} k_{ijkl} (s_{ij} - s_{0,ij}) (s_{kl} - s_{0,kl})$
Cross-coupling bond-angle	$E^{ba} = \sum_{ijk} k_{ijk} (r_{ij} - r_{0,ij}) (\theta_{ijk} - \theta_{0,ijk})$
Cross-coupling bond-torsion	$E^{bt} = \sum_{ijkl} (r_{ij} - r_{ij}^0) \sum_{m=1}^3 k_{(m)ijkl} \cos(m\varphi_{(m)ijkl})$
Cross-coupling angle-angle	$E^{aa} = \sum_{angleijk, anglejkl} k (\theta_{ijk} - \theta_{0,ijk}) (\theta_{jkl} - \theta_{0,jkl})$
Cross-coupling angle-torsion	$E^{at} = \sum_{ijkl} (\theta_{ijk} - \theta_{ijk}^0) \sum_{m=1}^3 k_{(m)ijkl} \cos(m\varphi_{(m)ijkl})$
Cross-coupling torsion-torsion	$E^{tt} = \sum_{ijklm} k_{ijklm} \cos(\varphi_{ijkl}) \cos(\varphi_{jklm})$
Van der Waals (Lennard-Jones)	$E^{vdw} = \sum_i \sum_{i \neq j} \epsilon_{ij} \left[2 \left(\frac{r_{ij}^0}{r_{ij}} \right)^9 - 3 \left(\frac{r_{ij}^0}{r_{ij}} \right)^6 \right] \text{if } r_{ij} \leq 12\text{\AA} E^{vdw} = 0 \text{if } r_{ij} > 12\text{\AA}$
Electrostatic (Coulomb)	$E^{coul} = \frac{1}{4\pi\epsilon_0} \sum_i \sum_{i \neq j} \frac{q_i q_j}{r_{ij}} \text{if } r_{ij} \leq 12\text{\AA} E^{coul} = 0 \text{if } r_{ij} > 12\text{\AA}$
Long Range Interactions	Particle-Particle Particle-Mesh Method with a k space style to a precision of 10^{-4} [30].

computational and one experimental configuration. Nevertheless, the primary requirement for a force field in this context is that it effectively captures the complex interactions typical of bituminous molecules, which often exhibit high molecular weight and conformational planarity. Ultimately, the central objective of this manuscript is to examine the characteristic time ratios that facilitate comparative analysis of seemingly identical phenomena across different set ups, either experimentally and/or computationally.

2.3. Model construction

The molecular systems investigated in this study consist of mixtures formed by combining single molecule types, selected from Table 1, resulting in 12 distinct samples. The atom count in these systems is limited to 30,000 – resulting in an average number of molecules equal to about 350. The LAMMPS stages used to prepare these systems into their final, condensed state, suitable for use in subsequent simulations, are outlined as follows:

1. The SMILES notations for the molecules are retrieved, and the RDKit Python module [34] is employed to initialize these molecules by generating multiple metastable conformers using **EmbedMultipleConfs()**. Each conformer is then optimized through RDKit's **Minimize()** function using the MMFF94 [35] force field. The conformer with the lowest energy is selected and saved as the stable molecular structure to be used in subsequent steps.
2. Multiple molecules are then evenly distributed in a low-density box with an initial density of 0.20 g/cm³, ensuring an even distribution and minimizing particle overlap by utilizing a low-discrepancy Sobol spatial distribution method.
3. The PCFF force field parameters and charges are assigned to the molecules using RDKit atomic descriptor functions (e.g., **atom.GetIsAromatic()** to identify if an atom is a member of an aromatic

ring or **atom.GetHybridization()** to identify an atom's hybridization state). The atomic differentiation rules used to define atomic types in the PCFF force field are available in the following reference: [29].

4. The atomic positions are optimized to minimize E_{PCFF} in Eq. (1) using the conjugate gradients method [36] until the energies and forces converge to magnitudes below 1.0.
5. The systems are compressed to the target density under NVT conditions over a period of 5 ns, applying a true strain rate of 1 %, with isotropic deformations applied to the simulation box every 1000 steps using LAMMPS's **fix deform** command. Compression is halted once the dimensions of the simulation box become approximately equal and the system density is equal to the density estimate of the sample reported in Table 1. At this point, subsequent NPT stages will allow the box dimensions to adjust gradually, guiding the system toward a more precise equilibrium volume/density.
6. The systems are then subjected to 50 NPT annealing cycles for equilibration, where the system temperature is varied sinusoidally by ± 25 % of the original equilibrium temperature with variable periods of oscillation ranging from 0.1 to 2 ns [37]. These annealing cycles serve to minimize residual stresses, reducing the likelihood of the resulting systems being trapped in metastable configurations, thereby encouraging convergence toward lower-energy equilibrium states and reducing the likelihood of generating systems with significant residual strain. This is particularly important, as higher-energy metastable configurations are known to significantly distort the magnitude of stress tensors, leading to artificially elevated values [38].
7. The density of the systems is stabilized at the equilibrium temperature and pressure through two consecutive 20 ns-long NPT stages. The final density is determined from the average density recorded during the second NPT stage. A sample simulation of Sample 1 (Squalane) can be found in the */zero-shear* directory of the **Supplementary Information**.
8. Dynamics stages are conducted under NVT and NVE conditions, each for a duration of 50 ns. These stages are designed to assess the stability of the systems without the influence of a barostat or thermostat, where the potential and kinetic energy should remain within 5 % of the initial (i.e., from Step 7) average. Step 8 is purely evaluative; systems that successfully pass this stage are selected from those that completed Step 7. Systems that fail to meet the criteria in this step necessitate that the building process be initiated again (from Step 1).

The initialization of molecular systems, corresponding to Steps 1 through 3, are performed using SMIPDB [39] and PDB2DAT [40], a collection of tools developed by our research team to facilitate the generation of molecular systems ready for use in LAMMPS. The thermostat and barostat employ a modified Nose-Hoover integration algorithm that includes a drag factor to mitigate oscillatory effects [41]. The pressure and temperature damping factors are set to 500 steps, and the particle velocity drag coefficient is maintained at 1.0. Each LAMMPS subroutine is run at a temperature of 25 °C and a pressure of 101325 Pa, with a step size of 0.5 fs/step unless otherwise indicated. Periodic boundary conditions are applied in all directions.

3. Oscillatory simulations setup

The way this paper aims to capture a viscoelastic response is by using oscillatory shear deformations to cyclically strain the simulation box and measure the resulting stress of the materials. The technique and conditions are similar to those reported by Ebrahimi et al. [42] and Ewen et al. [43]. A thorough description of the methodology, definitions, and simulation details are presented next.

3.1. Simulation box

MD simulations traditionally utilize orthogonal control volumes, characterized by cubical simulation boxes. The dimensions of these boxes are determined by the vertex distances (e.g., $l_x = x_{hi} - x_{lo}$). In these configurations, the tilt angles— α , β , and γ —are fixed at 90 degrees, resulting in zero tilt/shear factors. To simulate shearing deformations similar to those used in DMA tests, it is essential to perform simulations within a triclinic rhombohedral simulation box. In this case, the box maintains constant side lengths along the x, y, and z axes, while only the tilt angle γ is subject to oscillatory variation over time. Table 3 illustrates how the vertex positions (x_{hi} , x_{lo} , y_{hi} , y_{lo} , z_{hi} , and z_{lo}) correlate with the box's edge lengths and tilt angles in both orthogonal and triclinic rhombohedral configurations. Additionally, Table 3 presents the mathematical expressions employed to calculate these parameters throughout the simulations, facilitating the precise quantification and manipulation of shearing deformations in an initially cubic control volume.

3.2. Strain waveform

The waveform selected for the deformation test of this study has a sinewave form, where the xy-face of the simulation box is displaced along the x-direction as a function of simulation time, emulating shearing with no changes in volume throughout the simulation. The expression for this sinewave form, and thus for the shear strain applied ($\gamma(t)$) is given by Eq. (2),

$$\gamma(t) = l_{xy}(t) = \gamma_0 \sin(\omega t) \quad (2)$$

where γ_0 represents the amplitude of the strain wave divided by l_y , ω is the angular frequency given by $\omega = 2\pi f$, and t the instantaneous time. The sinewave is placed such that $\gamma(t = 0)$ equals to 0. Consequently, the shear strain rate ($\dot{\gamma}(t)$) is given by Eq. (3),

$$\dot{\gamma}(t) = \frac{d\gamma}{dt} = \omega \gamma_0 \cos(\omega t) \quad (3)$$

Sinewaves are effective in MD simulations because they facilitate a gradual increase in deformation, allowing for a smooth transition to

larger strains and preventing abrupt molecular responses. Moreover, a sine wave ensures constant variation in the strain rate applied, preventing the rapid relaxation of molecular conformations from adjusting to the shear rate applied, which can result in unrepresentative stress measurements in MD simulations [44].

For similar reasons, experimental DMA tests often employ sine functions to apply cyclic strain, as this waveform ensures a smooth, controlled application of deformation enticing a smooth (but delayed) stress response as well. Specifically, a sine function begins smoothly at zero strain, aligning with the system's undeformed equilibrium state and avoiding abrupt displacement as seen with other sinusoidal forms, such as cosine, which starts at a peak. This smooth onset minimizes non-equilibrium effects, supports simulation stability, and provides harmonic consistency that resonates naturally with molecular oscillations [4]. The sine function's symmetry also enables cyclic, reversible deformation without introducing phase shifts, while the controlled build-up of strain maintains molecular integrity, ensuring reliable stress-strain data throughout the simulation [45].

3.3. Stress definition

The stress tensors for each atom are calculated using the virial equation [46], which relates the stress to the atomic interactions within the system. The stress tensors are obtained using Eq. (4), defined as:

$$\sigma_{\alpha\beta} = \frac{1}{V} \left(\sum_i m_i v_{i\alpha} v_{i\beta} - \sum_{i<j} r_{ij\alpha} f_{ij\beta} \right) \quad (4)$$

where m_i denotes the mass of atom i , $v_{i\alpha}$ and $v_{i\beta}$ are the components of the velocity of atom i along the α and β directions, respectively, $r_{ij\alpha}$ is the α component of the distance vector between atoms i and j , $f_{ij\beta}$ is the β component of the force exerted by atom j on atom i , and V represents the volume of the simulation box.

The virial stress includes contributions from both kinetic and potential energy terms. The kinetic energy term, given by $\sum_i m_i v_{i\alpha} v_{i\beta}$, accounts for the momentum flux due to the motion of the atoms. The potential energy term, expressed as $\sum_{i<j} r_{ij\alpha} f_{ij\beta}$, represents the configurational forces arising from the interactions among atoms computed by

Table 3

Illustration and expressions used by LAMMPS correlating the simulation box's vertices with the box's edge lengths and tilt/shear factors. In these strain-controlled simulations, the l_{xy} strain component varies sinusoidally with time, while the l_{xz} and l_{yz} components are maintained at zero, ensuring deformation occurs only within the xy-plane.

Quantity	Expression
l_x	$x_{hi} - x_{lo}$
l_y	$y_{hi} - y_{lo}$
l_z	$z_{hi} - z_{lo}$
A	l_x
B	$\sqrt{l_y^2 + l_{xy}^2}$
C	$\sqrt{l_x^2 + l_{xz}^2 + l_{yz}^2}$
α	$\cos^{-1} \left(\frac{l_{xy} l_{xz} + l_y l_{yz}}{BC} \right)$
β	$\cos^{-1} \left(\frac{l_{xz}}{C} \right)$
γ	$\cos^{-1} \left(\frac{l_{xy}}{B} \right)$

the PCFF force field. These interactions include all contributions from bonded interactions such as bonds, angles, dihedrals, and impropers, as well as non-bonded interactions like Van der Waals and Coulomb forces, as show in Eq. (1). Therefore, the corresponding shear stress during the cyclic deformation tests of this study, denoted as σ_{xy} , is determined by Eq. (5) as follows:

$$\sigma_{xy} = \frac{1}{V} \left(\sum_i m_i v_{ix} v_{iy} - \sum_{i<j} r_{ij} f_{ijy} \right) \quad (5)$$

It is important to note that σ_{xy} reflects the combined impact of both inherent stresses within the material and stresses induced by applied shear deformation. The inherent stresses are present even in the absence of shear, arising from the dynamic fluctuations in the material's configuration and the pressure acting on the system. Additionally, σ_{xy} includes stresses generated by the shearing deformation applied to the material during the simulation, which correspond to the material's resistance to externally imposed shear forces.

3.4. Stress waveform

The resulting stress measurements, $\sigma_{xy}(t)$, throughout the simulations are expected to follow a sinusoidal form similar to the waveform of the strain applied. However, as is in the case of any non-elastic solid in strain-controlled cases, the stress response of these viscoelastic materials is expected to lag behind the strain applied. Therefore, $\sigma_{xy}(t)$ is expected to follow the form in Eq. (6):

$$\sigma_{xy}(t) = \sigma_0 \sin(\omega t + \delta) \quad (6)$$

where σ_0 corresponds to the amplitude of the stress wave, ω is the angular frequency (equal to that of $\gamma(t)$), t is the simulation time, and δ corresponds to the phase lag. A fundamental limitation of all-atom MD simulations arises when the amplitude of the measured shear stress, $\sigma_{xy}(t)$, approaches the magnitude of σ_{xy} under zero-shear conditions. This situation occurs as the deformation frequencies become progressively lower, making it statistically challenging to obtain a measurable stress response from the applied shearing deformation.

3.5. Dynamic properties

The complex modulus (G^*) is determined through the analysis of the material's linear response to a sinusoidal strain applied [47], as illustrated by Eq. (7):

$$\sigma(t) = G^*(t)\gamma(t) \quad (7)$$

The storage and the loss moduli, denoted as G' and G'' , are obtained by rewriting Eq. (7) into Eq. (8):

$$\sigma(t) = \gamma_0 G' \sin(\omega t) + \gamma_0 G'' \cos(\omega t) \quad (8)$$

where $G' = \frac{\sigma_0}{\gamma_0} \cos(\delta)$ and $G'' = \frac{\sigma_0}{\gamma_0} \sin(\delta)$. Both the storage and the loss modulus are then obtained by integrating each term in $\sigma(t)$ in Eq. (7) and Eq. (8). Therefore, $G'(\omega)$ and $G''(\omega)$ become, using Eq. (9) and Eq. (10),

$$G'(\omega) = \frac{\omega}{N_c \pi \gamma_0^2} \int_0^{2\pi N_c / \omega} \sigma(t) \gamma(t) dt \quad (9)$$

and

$$G''(\omega) = \frac{1}{N_c \pi \gamma_0^2} \int_0^{2\pi N_c / \omega} \sigma(t) \dot{\gamma}(t) dt \quad (10)$$

where N_c is the number of cycles (or periods) applied and dt corresponds to the sampling time, in this case, for $\sigma_{xy}(t)$ (Note: the sampling time is not equal to the simulation time step – it corresponds to how often stress measurements are captured and recorded throughout a simulation).

Given a sufficient resolution of samples, Eqs. (9) and (10) can be approximated by Eqs. (11) and (12),

$$G'(\omega) = \frac{\omega}{N_c \pi \gamma_0^2} \sum_i \sigma(t) \gamma(t) dt \quad (11)$$

and

$$G''(\omega) = \frac{1}{N_c \pi \gamma_0^2} \sum_i \sigma(t) \dot{\gamma}(t) dt \quad (12)$$

The complex modulus, G^* , which combines the impact of G' and G'' into one metric, is given by Eq. (13),

$$G^*(\omega) = \sqrt{G'(\omega)^2 + G''(\omega)^2}. \quad (13)$$

More reliable indicators of the viscoelastic response of the materials tested are the storage (η'), loss (η''), and the complex (η^*) viscosities, given in Eq. (14), Eq. (15), and Eq. (16) respectively, as follows:

$$\eta'(\omega) = \frac{G'(\omega)}{\omega} \quad (14)$$

$$\eta''(\omega) = \frac{G''(\omega)}{\omega} \quad (15)$$

and

$$\eta^*(\omega) = \frac{G^*(\omega)}{\omega} \quad (16)$$

These are often reported in experimental oscillatory tests and can serve as appropriate indicators of the rheological response of the materials under different temperatures and frequencies.

These metrics characterize the mechanical response of a material under different strain rates and temperatures. Broadly, the materials in this study can be categorized into four types: (1) Stiff Elastic materials, which strongly resist deformation and largely recover their original shape after deformation; (2) Soft Elastic materials, which weakly resist deformation but still largely recover their original form when deformed; (3) Thick Viscous materials, which offer strong resistance to deformation but do not recover their shape once deformed; and (4) Thin Viscous materials, which weakly resist deformation and, once deformed, do not recover their original shape. Table 4 displays examples of common materials categorized by their typical mechanical response. Viscoelastic materials like bitumen exhibit characteristics of all four categories, some becoming more dominant as the conditions to which they are subjected change.

3.6. Characteristic time

The characteristic time (τ) of a molecular system is defined as the observed time over which the system dissipates stress and returns to equilibrium following the application and release of a perturbation. Various characteristic times can be identified, each corresponding to different perturbation phenomena (e.g., shearing deformation or a

Table 4

Examples of materials categorized by mechanical response, showing values for Storage Modulus (G') and Loss Modulus (G'') under typical operating conditions.

Material Type	Real-Life Example	Typical G' (Storage Modulus) [MPa]	Typical G'' (Loss Modulus) [MPa]
Stiff Elastic	Steel, Aluminium	1000	10
Soft Elastic	Rubber Band, Silicone, Latex	1	0.1
Thick Viscous	Asphalt Pavement, Wax, Resins	0.5	5
Thin Viscous	Water, Glycerol, Light Oils	<0.001	0.001

thermal perturbation) and stress-dissipation modes present in the system (e.g., an energy control scheme such as a barostat or a thermostat) [48]. In the simulations conducted in this study, τ is defined as the observed period of oscillation required to produce a balanced combination of viscous and elastic responses, achieved when the magnitudes of the loss modulus and the storage modulus are equal ($G'' = G'$).

Prior identification of the relaxation time is crucial for selecting the appropriate range of shearing frequencies to produce a comprehensive viscoelastic response envelope (where both G' and G'' play an influential role), given that the frequencies to produce such values of G' and G'' are initially unknown in the context of MD simulations. Testing only low relative deformation frequencies (significantly lower than $1/\tau$) would only yield fully viscous responses ($G'' \gg G'$), whereas testing only high relative frequencies (well beyond $1/\tau$) would elicit purely elastic responses ($G' \gg G''$) [49].

Moreover, obtaining an approximate value of τ aids in addressing, a priori, the time scale discrepancies that exist between MD and experimental phenomena of the same kind [43]. For example, the selection of frequency values for use in simulations involving bituminous materials is not straightforward as the experimental frequency range commonly used to test bitumens in laboratory conditions ($0.01\text{--}100\text{ s}^{-1}$ [45]) would correspond to about 10^{13} to 10^{17} simulation steps in all-atom simulations. This time scale initially suggests that replicating real-life frequency timescales in molecular simulations is unfeasible due to the large number of simulation steps. However, molecular phenomena often stabilize at a faster rate than observable in experiments (as $\tau \ll \tau_{exp}$), as denoted by other MD-related studies [50,51]. This accelerated stabilization allows the simulations to reflect relevant responses within computationally tractable durations (significantly fewer than 10^{13} steps) but introduces a discrepancy between the timescales of all-atom simulations dictated by the PCFF force field and real-world phenomena.

The relaxation time of multiple polymeric blends resembling those in Table 1 is reported to be equal to about $\tau = 100$ picoseconds in MD simulations [52]. While this value may not precisely reflect the deformation phenomenon under investigation—potentially necessitating a more accurate estimate—it provides a reasonable initial estimate for conducting exploratory sweep tests to characterize the viscoelastic response of the materials examined.

In the study of the 12 samples, multiple crossover points are expected to be observed within a single material, making it challenging to determine a single dominant relaxation time across all samples. In this paper, the value of $\tau = 100$ picoseconds is refined with a set of Section 4.1 by identifying the crossover point nearest to the transition between the Elastic and Glassy regions, where the loss modulus (G'') is also close to its absolute maximum. Although experimental methods often use relaxation times in the Rubbery and Viscous regions, identifying τ closer to the Elastic region is advantageous for MD simulations. This is because it corresponds to the point where internal energy dissipation, in nominal terms, is most significant. Moreover, the characteristic regions are expected to occur more rapidly in MD – closer to the onset of the Glassy region – requiring the sweep test to be skewed towards more elastic regimes.

4. Oscillatory simulations routines

The simulations involving shearing deformation cycles involve two LAMMPS subroutines run in series. The first subroutine corresponds to a continuation of Step 7 of the Section 2.3, comprised of an NPT simulation 5 million steps long, that serves to initialize the molecular models with the custom magnitude of the time step used for that particular test of the frequency sweep. The dimensions of the simulation box at the end of this stage are fixed to the average of the instantaneous dimensions recorded from the last 1 million steps. The second subroutine comprises the simulation involving shearing deformations, which deforms the simulation box following the waveform γ described earlier in this article

using LAMMPS's **fix deform** command at a defined frequency f_i . Subroutine 2 comprises n_c cycles, with each simulation involving a total simulation time of $t = \frac{n_c}{f_i}$.

To correctly obtain instantaneous values of $\sigma_{xy}(t)$ in the deformation simulations of Subroutine 2, given the difference in magnitude of the frequencies tested, simulations whose deformation frequencies are fast are capped to 100,000 simulation steps. This way, simulations involving faster frequencies are subject to timesteps that are proportionally shorter, and those with slower frequencies are run with longer time steps, thus capturing $\sigma_{xy}(t)$ values evenly regardless of the frequency magnitude tested. Maintaining an integration time step that resolves at least 10 steps within the fastest vibrational mode of the system is essential to ensure smooth trajectories and prevent numerical artifacts.

However, the fastest vibrational mode in the system, particularly as strain rates become less influential, corresponds to the oscillation period of C–H bonds, approximately 11 fs [51]. This imposes an inherent timescale limitation of molecular simulations involving all-atom PCFF dynamics, necessitating a time step equal to a maximum of 1 fs, regardless of the shearing conditions applied. This limitation forces simulations involving low deformation frequencies to have an increased number of simulation steps and thus an increased number of $\sigma_{xy}(t)$ samples, thereby improving the statistical significance of the obtained stress values as these values are expected to decrease with decreasing deformation frequencies.

The motion of atoms in simulations of Subroutine 1 and 2, is derived from integrating the SLLOD equations of motion using LAMMPS' **fix nvt/sllod** command, which, unlike more conventional Nose-Hoover integration algorithms, modify the velocity of the atoms to account for the imposed strain rates, ensuring accurate stress tensor calculations and proper temperature control under shearing deformation conditions [53]. The dynamic value of the timestep (e.g., faster frequency deformations are performed with smaller timesteps) allows for an even control of the temperature while keeping the control value at once every 100 steps for all the simulations performed, especially required in simulations involving high frequencies expected to undergo significant temperature changes unless strictly controlled.

While the SLLOD thermostat already minimizes the explicit perturbation of the particles' velocities due to the applied strain, it still relies on introducing artificial perturbations to the motion of the particles to control their temperature [53]. For this reason, avoiding capturing the values of $\sigma_{xy}(t)$ right after the control step has been applied is essential. Conversely, capturing the values right before the control has been applied would yield the opposite effect; the particles are the furthest away from the control temperature [54]. Therefore, the values of $\sigma_{xy}(t)$ 25 steps before and after the applied control are discarded, minimizing the impact of the thermostat in the sampling while still maintaining a quasi-isothermal simulation regime.

There are two types of shearing deformation simulations performed in this study. The ones presented in Section 4.1 are used to tune the input parameters necessary for producing a comprehensive viscoelastic response centered around τ and an acceptable strain amplitude. The ones presented in Section 4.2 aim to generate an envelope of responses encompassing multiple characteristic regions (e.g., Elastic, Glassy, Viscous) with enough detail, enabling the generation of master curves, and the proper identification of the materials' viscoelastic properties.

4.1. Exploratory simulations

The Exploratory simulations sweep through a preliminary but wide range of frequencies to enhance the value of τ and thus obtain a narrower range of frequencies where the materials exhibit a viscoelastic response (see Section 3.6). Given the wide range of potential frequencies, only two models—representing the extremes of the most viscous and most elastic responses expected—are tested to capture a frequency envelope that encompasses all the materials and conditions

examined in this study. Specifically, Squalane (Molecule 1 from Table 1) tested at 200 °C, anticipated to exhibit the softest and most viscous response, and Thiophenic Asphaltene (Molecule 12 from Table 1) tested at 25 °C expected to exhibit the stiffest and most elastic response. These exploratory simulations are limited to three cycles ($n_{cycles} = 3$) to reduce the overall simulation time and resources required. The preliminary set of testing frequencies is generated by creating an array of 30 values, logarithmically distributed across nine orders of magnitude around $\tau = 100$ picoseconds.

The exploratory simulations also involve repeating the frequency sweep tests across four strain amplitudes γ_0 equal to 0.1, 1.0, 5.0, and 10 %, as for experimental tests, γ_0 often lies between 0.1 and 10 % for 25 and 200 °C respectively [25]. The selection of shear strain amplitudes is not expected to be subject to the fundamental scaling disparities encountered when choosing frequency ranges [51]. However, if the amplitude of the stress response sampled is too small, its magnitude would lie within the instantaneous variation of $\sigma_{xy}(t)$ under zero-shear conditions (obtained during Step 7 in the Section 2.3). Conversely, if the amplitude is too large, the test would no longer fall within the material's linear viscoelastic response regime, where an increase in γ_0 would not elicit a proportional increase in the magnitude of σ_{xy} , thereby invalidating the rheological analysis of Section 3.5. Remaining within the linear response regime is also critical as it allows for the use of a single strain amplitude value in all simulations, eliminating the need for a strain amplitude sweep test in subsequent simulations and reducing the number of cases to be tested [45].

4.2. Detailed simulations

The Detailed Simulations involve performing the cyclic shearing deformation tests through all the compounds of Table 1, at a single strain level (γ_0 equal to 5 %), and at different temperatures and frequencies centered around $\tau = (\tau_{squalane} + \tau_{thiophene})/2$ (τ left at 100 ps), to capture their viscoelastic response envelope more accurately. In this study, 5 different temperatures are evaluated: 25, 60, 120, 135, and 200 °C. These temperatures are deliberately chosen as they represent commonly used points to test bituminous materials (both in the lab and during applications) and have been found to engulf multiple characteristic regions (e.g., Elastic, Glassy, Rubbery, and Viscous). Moreover, plenty of experimental data is available at these specific temperatures to further evaluate the application of these models when compared to real-life sample observations.

The sweep of frequency values consists of a total of 20 points distributed logarithmically, covering a range spanning seven orders of magnitude. These values are centered around the updated value of τ obtained from Section 4.1, and are equal to 1.000, 2.33, 5.45, 12.7, 29.7, 69.4, 162, 378, 884, 2060, 4820, 11,300, 26,300, 61,500, 144,000, 336,000, 785,000, 1,830,000, 4,280,000, 10,000,000 fs. While experimentally obtained master curves often span over a broader frequency range (e.g., often spanning over 10 orders of magnitude), the Time-Temperature Superposition (TTS) principle will be used to combine the results from different temperatures to obtain a broader, more representative master curve. The number of cycles is increased to $n_{cycles} = 10$, from which only the last 5 are used for analysis to avoid incorporating initialization effects (e.g., residual stresses). Directory `/sample_oscillatory_simulation` contains the necessary LAMMPS scripts needed to perform an oscillatory deformation simulation of Squalane at 25 °C and a cycle's period of oscillation equal to 1.000 fs.

5. Benchmarking properties

5.1. Thermophysical

Even though this manuscript aims to capture stress-related properties, some fundamental thermophysical properties are obtained to 1)

check whether the MD models are built correctly and lack numerical instabilities, 2) evaluate fundamental thermodynamic properties to make sure the models more likely correspond to the materials they are used to model, and 3) to have some quantities to fall back to if there are considerable discrepancies found in force-related benchmarks, allowing to find the probable cause of the discrepancy by comparing more fundamental properties between models and experimental observations. These properties are listed in Table 5.

5.2. Stress-related

In this study, two types of stress-related properties are measured: those intrinsic to the material under no-shear conditions, and those obtained during oscillatory deformation tests. The no-shear properties confirm the accuracy of the model's construction and initialization, such as verifying that residual stresses from molecular interlocking do not significantly impact stress measurements. Additionally, these properties address the inherent limitation noted in Section 3.4 under low-frequency deformation conditions, where stress values at very low frequencies are expected to converge with those observed under zero-shear conditions. The intrinsic stress properties are presented in Table 6.

The properties obtained during the oscillatory deformation tests are summarized in Table 7. These amount to six properties – G' , G'' , G^* , η' , η'' , η^* – which are essential in DMA-related studies describing the rheology of viscoelastic materials.

6. Results

The Results section of this manuscript starts by presenting the thermodynamic and stress-related properties of the systems obtained in no-shear conditions (Section 6.1). It then proceeds to present the results of the oscillatory deformation tests (Section 6.2).

6.1. No-shear conditions

Table 8 presents the thermophysical properties—density, heat of vaporization, heat capacity, solubility parameter, and thermal expansion coefficient—measured under no-shear conditions. Table 9 provides stress-related properties under similar conditions. The properties in the latter are reported with their variability—to one standard deviation. The variability, especially of σ_{xy} , aims to establish the force field's ability to capture near zero-shear stresses, below which stress measurements captured using explicit deformations fall below the no-shear regime,

Table 5

Zero-shear thermophysical properties used to evaluate whether the MD systems realistically model the molecules of this study.

Quantity	Expression	Notes
Potential Energy (P_E) [kJ/kg]	E_{PCFF}	From force field expression (Eq. (1))
Molar Volume (V_m) [m ³]	$V_m = \frac{M_w}{\rho}$	Obtained from the average of the second NPT run in Step 7 of the Section 2.3.
Density (ρ) [kg/m ³]	$\rho = \frac{m}{V}$	
Self-diffusion coefficient (D) [m ² /s]	$D = \lim_{n \rightarrow \infty} \frac{ \mathbf{r}(t) - \mathbf{r}(0) ^2}{6t}$	
Enthalpy of Vaporization (H_v) [kJ/kg]	$H_v = V_m CED + RT$	Obtained from an additional run to obtain the CED. Simulation details available in the Supplementary Information, CED.docx.
Solubility Parameter (δ_{sol}) [kJ ^{0.5} /m ^{1.5}]	$\delta_{sol} = \sqrt{\frac{CED}{V_m}}$	
Isochoric Heat Capacity (C_v) [kJ/kg/K]	$C_v = \left(\frac{\delta U}{\delta T}\right)_V$	Obtained by capturing internal energy fluctuations during the thermal cycling of Step 5 in the Section 2.3.
Thermal Expansion Coefficient (β) [1/K]	$\beta = \frac{1}{V} \left(\frac{\delta V}{\delta T}\right)_P$	

Table 6

Zero-shear force-related properties used to evaluate the stability of the stresses in the systems prior to performing the oscillatory deformation tests.

Quantity	Expression	Notes
No shear stress tensors ($\sigma_{\alpha,\beta}$) [MPa]	$\sigma_{xx}, \sigma_{yy}, \sigma_{zz}, \sigma_{xy}, \sigma_{xz},$ and σ_{yz}	Obtained by computing the average of $\sigma_{\alpha,\beta}$ during the second NPT run in Step 7 of the Section 2.3 .
Pressure (P) [MPa]	$P = -\frac{1}{3V}(\sigma_{xx} + \sigma_{yy} + \sigma_{zz})$	
Surface Tension (T) [N/m]	$T = \frac{l_z}{2} \left(\frac{\sigma_{xx} + \sigma_{yy}}{2} - \sigma_{zz} \right)$	

Table 7

Seven properties – the dynamic moduli, their corresponding viscosities, and the material's characteristic time – are computed after performing the oscillatory deformation tests.

Quantity	Expression	Notes
Storage Modulus (G') [Pa]	$G'(\omega) = \frac{\omega}{N_c \pi \gamma_0^2} \sum_t \sigma(t) \dot{\gamma}(t) dt$	Obtained after completing the Section 4.2 . Details of their computation can be found in Section 3.5 and Section 3.6
Loss Modulus (G'') [Pa]	$G''(\omega) = \frac{1}{N_c \pi \gamma_0^2} \sum_t \sigma(t) \dot{\gamma}(t) dt$	
Complex Modulus (G^*) [Pa]	$G^*(\omega) = \sqrt{G'(\omega)^2 + G''(\omega)^2}$	
Complex Viscosity (η) [Pa.s]	$\eta(\omega) = \frac{G^*}{\omega}$	
Storage Viscosity (η') [Pa.s]	$\eta'(\omega) = \frac{G'}{\omega}$	
Loss Viscosity (η'') [Pa.s]	$\eta''(\omega) = \frac{G''}{\omega}$	

becoming statistically irrelevant.

6.2. Oscillatory shear conditions

Capturing the dynamic moduli (G' , G'' , and G^*) and their corresponding viscosities (η' , η'' , and η^*) involves producing frequency-dependent curves that showcase their dependency on frequency and temperature. These plots provide a comprehensive description of the material's response. However, four simplifications are applied to capture the dynamic properties in a manner that can convey a general response of the material through four single quantities. This approach allows for quick comparative assessments between samples before focusing on the more complicated nature of characterizing materials based on the frequency-dependent dynamic properties.

Table 8

Thermodynamic properties obtained computationally and experimentally under no-shear conditions.

Model	Type	Experimental					Computational				
		ρ [kg/m ³]	H_v [kJ/kg]	C_p [kJ/kg/K]	δ_{sol} [kJ ^{0.5} /m ^{1.5}]	β [1/K]	ρ [kg/m ³]	H_v [kJ/kg]	C_p [kJ/kg/K]	δ_{sol} [kJ ^{0.5} /m ^{1.5}]	β [1/K]
		[55,56]	[55,57]	[58,59]	[60]	(•10 ⁴)[61]					(•10 ⁴)
1	Saturates	850	270–290	2.0–3.0	509.9	5–8	799	305.6	2.47	8.51	8.51
2		945	261.0	2.56	2.75	2.75					
3	Aromatics	1000	300	1.5–2.0	631.6	4–7	926	337.6	2.42	4.03	4.03
4		1007	317.2	2.13	10.7	10.7					
5	Resins	1050	300	1.5–2.0	618.9	1–4	999	265.1	2.26	3.07	3.07
6		967	319.6	2.24	2.34	2.34					
7		1013	333.7	2.05	2.41	2.41					
8		1341	424.2	1.26	3.94	3.94					
9		1025	262.4	2.18	4.37	4.37					
10		Asphaltenes	1070	350–450	1.0–1.5	575.8	0.1–1.5	999	327.1	2.15	2.76
11	968		290.6	2.09	2.44	2.44					
12	1054		321.4	1.93	2.75	2.75					

First, y_1 is determined by computing the logarithmic mean of all the y values across the frequencies tested, capturing an overall average of the properties. Second, y_2 is obtained by taking the logarithmic mean of the three y values corresponding to the lowest frequencies, expressing y under near zero-shear conditions, where the frequency of deformation is at its lowest. Third, y_3 is captured as the mean of the y values closest to the logarithmic middle point of the frequencies tested, equal to the updated value of τ , to equally capture both viscous and elastic responses in one value. Finally, y_4 is captured at the frequency where the storage modulus is at its maximum, showcasing the point where the most viscous energy is dissipated.

A temperature susceptibility factor is also reported to capture how the dynamic properties are expected to decrease when subjected to an increase in temperature, in this case from 25 to 200 °C. This factor, denoted by χ , is given in Eq. [17](#) as:

$$\chi = \frac{y_{200C}}{y_{25C}}$$

where y is one of the dynamic properties – G' , G'' , G^* , η' , η'' , or η^* . A higher value of χ indicates greater thermal susceptibility of the material with respect to metric y .

The metrics y_1 , y_2 , y_3 , y_4 , and χ , though straightforward, enable a quick, comparative assessment of the rheological responses of the tested samples without the need for an in-depth analysis of their master curves (e.g., quickly identifying which compounds exhibit greater stiffness or softness, or varying thickness).

[Table 10](#) presents the dynamic moduli (G' , G'' , and G^*) and their corresponding viscosities (η' , η'' , and η^*) obtained using the second approach (y_2) grouped by SARA fraction at 25 and 200 °C. y_2 is chosen because the magnitudes of the dynamic moduli within this frequency range compare well to those obtained experimentally, thus potentially providing realistically meaningful measurements comparable to those obtained in laboratory conditions.

[Table 11](#) captures the thermal susceptibility of the dynamic moduli (G' , G'' , and G^*) and their corresponding viscosities (η' , η'' , and η^*) by showing the ratio of said properties – obtained using the second approach – at 25 and 200 °C for each SARA fraction. A comprehensive list of thermal susceptibility factors χ , for all samples, obtained using metrics y_1 through y_4 , is available in the [Supplementary Information](#), file *thermal_susceptibility_chi.csv*.

A comprehensive list of the dynamic moduli (G' , G'' , and G^*) and their viscosities (η' , η'' , and η^*) for all the samples measured using both Metrics y_1 through y_4 , both at 25 and 200 °C is available in the [Supplementary Information](#), File *dynamic_properties_1-12.csv*.

[Table 12](#) displays frequency dependence plots of the dynamic properties (G' , G'' , and G^*) and their corresponding viscosities (η' , η'' , and η^*) at 25 °C. The plots present the properties for SARA fractions instead

Table 9

Stress-related properties obtained under no-shear conditions. Although no external stress is applied, the molecular systems still exhibit instantaneous variations in these stress-related properties, which proves valuable in assessing the force field's ability to capture near zero-shear stresses response.

Model	Type	P [MPa]	σ_{xy} [MPa]	σ_{xz} [MPa]	σ_{yz} [MPa]	T [N/m]
1	Saturates	0.13 ± 11	2.4 ± 27	2.7 ± 25	2.4 ± 26	0.025 ± 0.086
2		0.11 ± 12	9.5 ± 31	5.7 ± 31	4 ± 31	0.018 ± 0.1
3	Aromatics	0.07 ± 8.6	10 ± 32	6.2 ± 31	12 ± 32	0.024 ± 0.1
4		0.12 ± 8.9	2.4 ± 32	7.0 ± 30	6.8 ± 30	0.016 ± 0.1
5	Resins	0.11 ± 8.8	6.7 ± 32	0.27 ± 29	4.7 ± 30	0.035 ± 0.1
6		0.083 ± 11	6.7 ± 32	4.5 ± 31	9.4 ± 31	0.027 ± 0.1
7		0.11 ± 9.7	2.7 ± 30	3.9 ± 28	9 ± 28	0.038 ± 0.093
8		0.094 ± 7.6	3.8 ± 28	0.032 ± 29	2.4 ± 32	0.036 ± 0.11
9		0.11 ± 10	0.94 ± 28	8.3 ± 28	4.6 ± 28	0.0039 ± 0.094
10	Asphaltenes	0.096 ± 11	7.4 ± 32	9.3 ± 31	11 ± 32	0.0018 ± 0.1
11		0.086 ± 9.5	5.9 ± 30	2.5 ± 28	3.7 ± 28	0.0021 ± 0.093
12		0.08 ± 8.9	7.5 ± 32	0.201 ± 31	2.9 ± 30	0.0020 ± 0.099

Table 10

Dynamic moduli (G' , G'' , and G^*) and their corresponding viscosities (η' , η'' , and η^*) obtained using the first and second approach (y_1 and y_2) grouped by SARA fraction at 25 and 200 °C.

SARA	Temperature [°C]	G'_2 [MPa]	G''_2 [MPa]	G^*_2 [MPa]	η'_2 [Pa.s]	η''_2 [Pa.s]	η^*_2 [Pa.s]
Saturate	25	3145	1421	3643	2.143	0.9687	2.482
Aromatic		4555	3239	5792	3.103	2.207	3.946
Resin		11,982	3246	12,794	7.669	1.978	8.177
Asphaltene		12,158	4502	13,200	8.287	3.067	9.001
Saturate	200	97.53	59.1	123.7	0.0664	0.0402	0.0842
Aromatic		89.87	87.01	147.3	0.0612	0.0592	0.1003
Resin		309.2	403.5	537.8	0.2103	0.2745	0.3659
Asphaltene		1579	1447	2183	1.076	0.9859	1.487

Table 11

Thermal susceptibility factors of the dynamic moduli (G' , G'' , and G^*) and their corresponding viscosities (η' , η'' , and η^*) from 25C and 200C.

SARA	G'_2 [MPa]	G''_2 [MPa]	G^*_2 [MPa]	η'_2 [Pa.s]	η''_2 [Pa.s]	η^*_2 [Pa.s]
Saturates	0.19	0.04	0.07	0.19	0.04	0.07
Aromatics	0.02	0.03	0.03	0.02	0.03	0.03
Resins	0.05	0.20	0.05	0.05	0.20	0.05
Asphaltenes	0.15	0.32	0.17	0.15	0.32	0.17

of all samples for simplicity. Table 13 provides analogous data at 200 °C to illustrate the temperature dependency of these properties. The plots in Table 12 and Table 13 have not been merged using the TTS principle, as this method is not suitable for predominantly elastic responses, to preserve the characteristics of the materials within less linear, high-frequency regimes. Analogous plots, for Samples 1 through 12, at 25 and 200 °C, are available in the `/frequency_dependent_plots` directory in the [Supplementary Information](#). Analogous data, organized in CSV files, can be found in the `/frequency_dependent_data` directory.

Table 14 consolidates the data from Table 12 (measured at 25 °C) and Table 13 (measured at 200 °C) using the TTS principle. Specifically, the last five lowest frequencies tested at 200 °C, where the material response is predominantly linear and suitable for TTS extrapolation, are incorporated into the 25 °C plots and shifted accordingly. Despite the inclusion of only five additional frequencies, the frequency domain is significantly extended, from 10^{-7} to 10^{-9} fs^{-1} , corresponding to a period of oscillation increase from 10 ns to 1 microsecond. This extension reaches a time scale that is rarely, if ever, achieved using all-atom MD simulations of bitumen.

The frequency-dependent plots reveal multiple characteristic re-

gions, which help determine if the tested frequency range encompasses different response regimes, similar to those observed in experimental settings. This analysis aims to demonstrate whether the nominally high frequencies used in simulations can mimic the material responses typically seen at much lower frequencies in real life. These identified regions can then be used to establish timescale equivalencies between MD and experimental times, compare physical responses between samples and SARA fractions, and assess if the tested frequency range captures the typical viscoelastic response regimes of hydrocarbon materials. There are five distinct regions [62], listed from high to low frequency: Elastic, Glassy, Rubbery, Rubbery Flow, and Viscous Flow, as reported in multiple studies exploring the viscoelastic response of polymers and hydrocarbon blends [63,64]. Each characteristic point, numbered 1 to 4, marks the beginning of each region in descending frequency order (e.g., Point 1 denotes the onset of the Glassy region). This approach is only applied on the TTS-induced plots of Table 14 – as these encompass the broadest range of frequencies tested – capturing the characteristic points of SARA fraction samples across frequencies ranging from 10^0 to 10^{-9} fs^{-1} .

Fig. 1 showcases G^* and η^* across all frequencies (TTS included) for each SARA fraction. Multiple characteristic regions show up within the frequencies tested. The frequency ranges that correspond to these characteristic regions can be compared to those that have been identified experimentally [65]. Fig. 2 merges the master curves of G^* obtained from Table 14 for each SARA fraction with the master curve obtained by Catsiff and Tobolski on Polyisobutylene [66]. Although Polyisobutylene is not strictly related to bitumen, it exhibits comparable dynamic properties and characteristic times (e.g., a balanced viscous and elastic response, a Rubbery region centered at about 1 s^{-1} , viscosities of about 0.1–10 Pa s and moduli of 10–200 MPa). Moreover, the master curve obtained experimentally for Polyisobutylene is among the very few that

Table 12

Frequency dependency plots of the dynamic properties (G' , G'' , and G^*) depicted in red and their corresponding viscosities (η' , η'' , and η^*) depicted in blue at 25 °C. Complex, Storage, and Loss values in dark, intermediate, and light shades respectively.

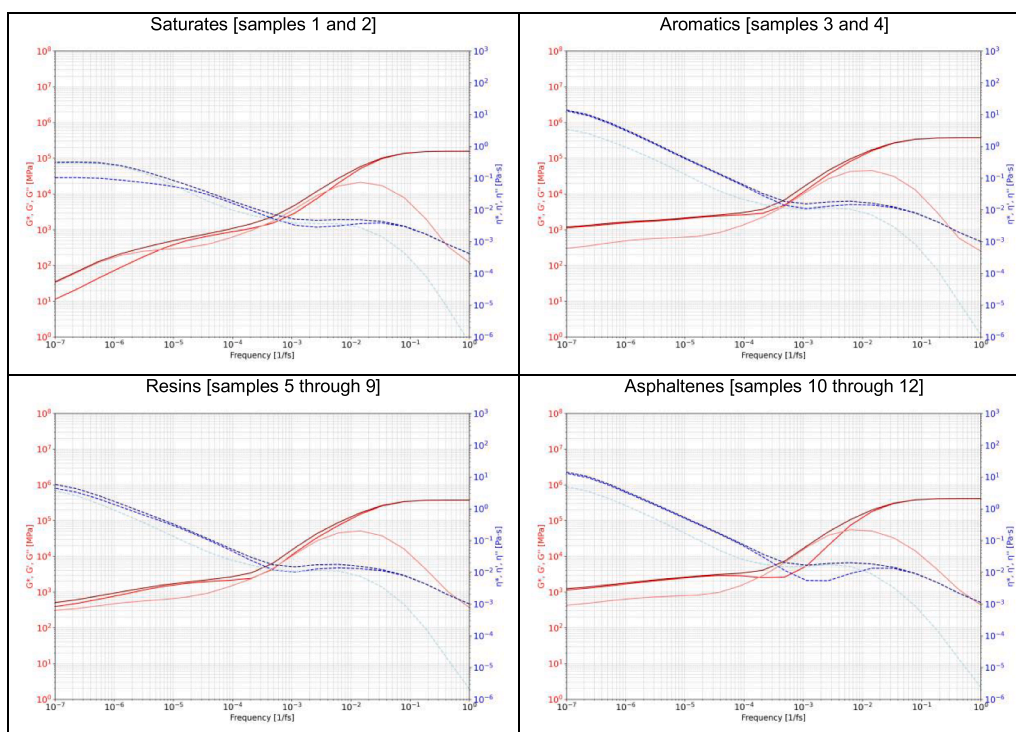


Table 13

Frequency dependency plots of the dynamic properties (G' , G'' , and G^*) depicted in red and their corresponding viscosities (η' , η'' , and η^*) depicted in blue at 200 °C. Complex, Storage, and Loss values in dark, intermediate, and light shades respectively.

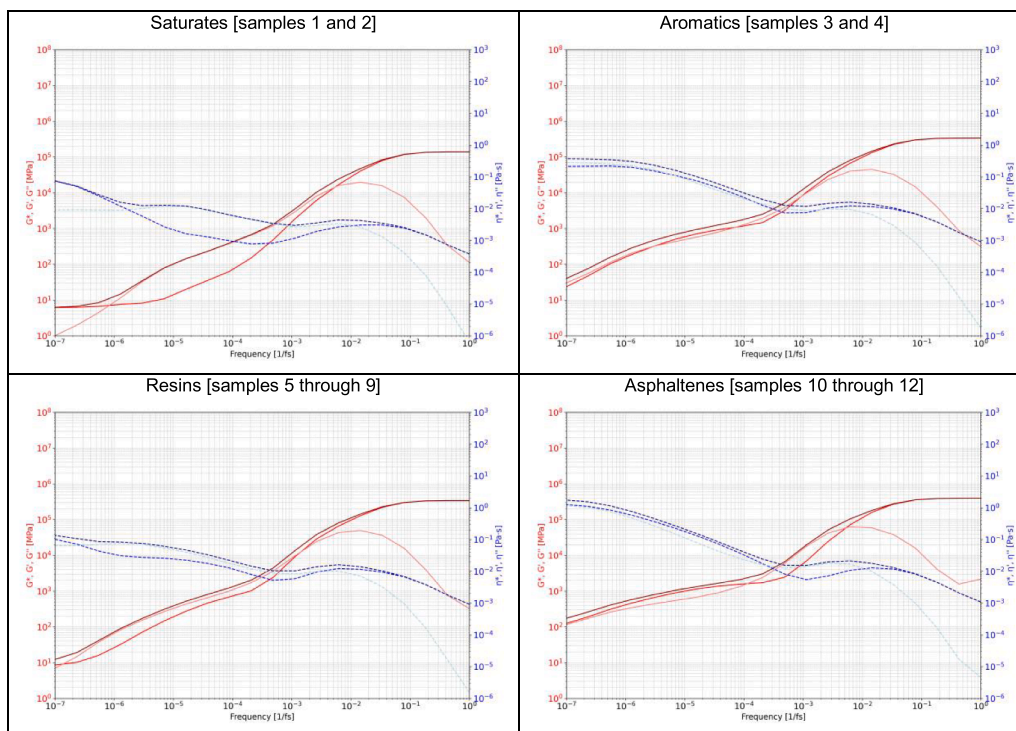


Table 14

Frequency dependency plots of the dynamic properties (G' , G'' , and G^*), depicted in red, and their corresponding viscosities (η' , η'' , and η^*), depicted in blue, extended from 10^{-7} to 10^{-9} fs $^{-1}$ (from the nanosecond to the microsecond domain) using the TTS principle. The vertical dashed line represents the boundary beyond which the results are derived from the TTS-induced shift. Complex, Storage, and Loss values in dark, intermediate, and light shades respectively.

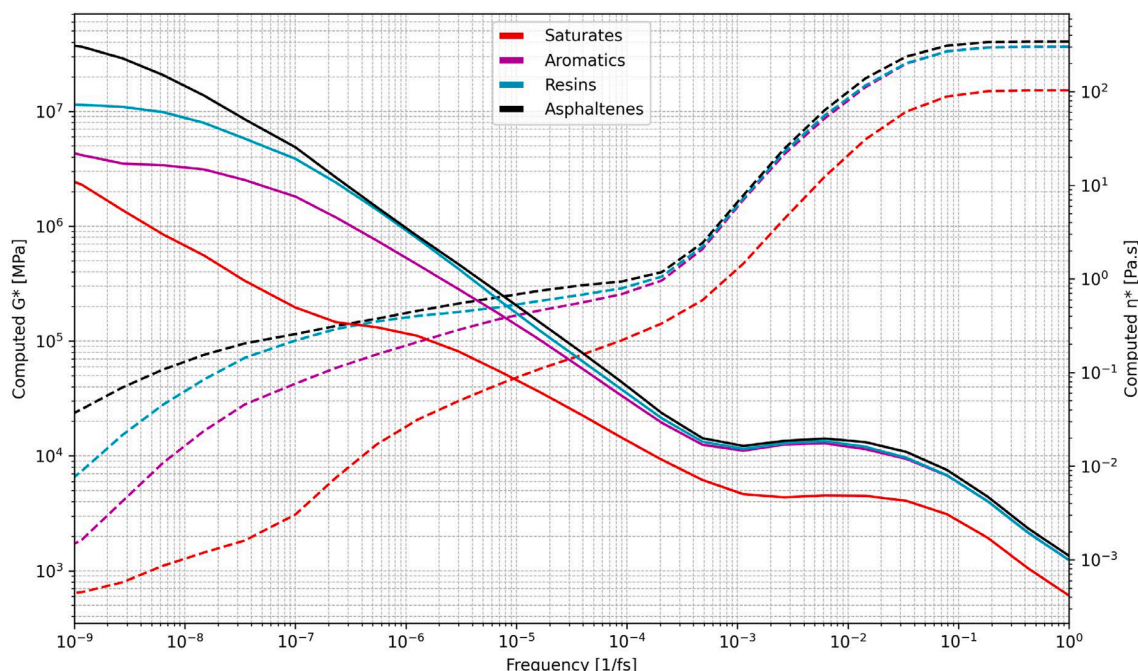
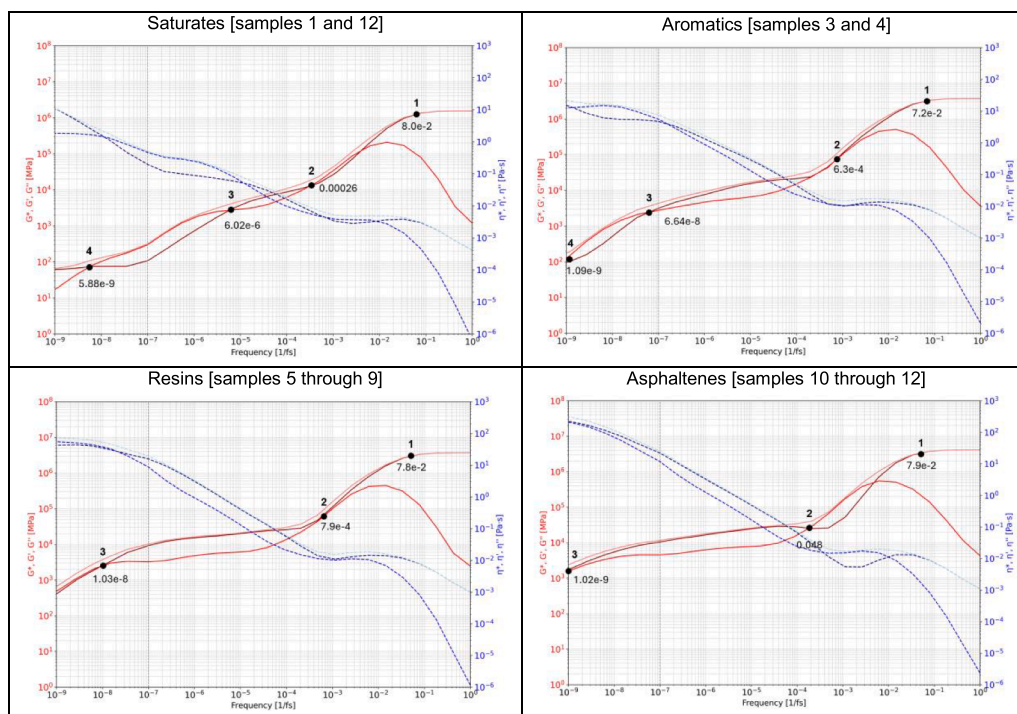


Fig. 1. Mastercurves of G^* (solid) and η^* (dashed) from Table 14 for each SARA fraction.

span 18 decades, depicting all characteristic regions of a complex hydrocarbon clearly. Table 15 displays the frequency range for each region in s $^{-1}$ and in fs $^{-1}$, comparing both experimentally and computationally

observed regions at 25 °C, and showcasing the time shift required to compare response regimes of similar nature between simulations and experimental observations.

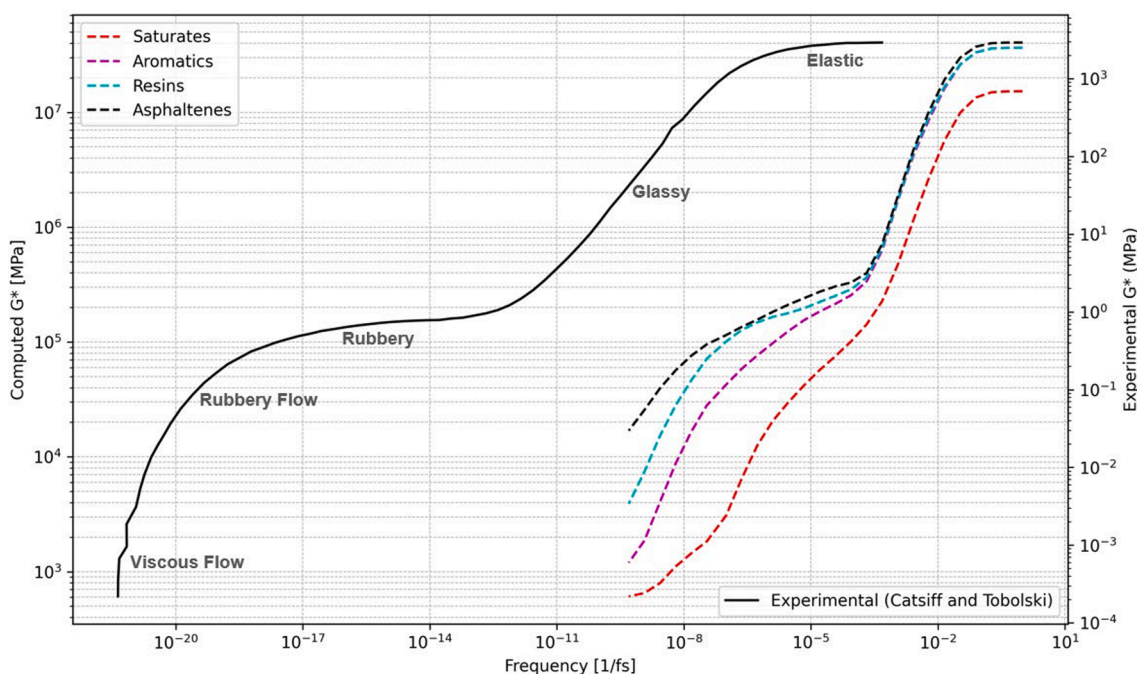


Fig. 2. Mastercurves of G^* from Table 14 in place with the experimentally obtained G^* values for Polyisobutylene by Catsiff and Tobolski [66].

Table 15

Frequency ranges for all 5 Characteristic regions for both experimental and MD samples of bitumen at 25 °C.

Region	Experimental [s ⁻¹]	Experimental [fs ⁻¹]	MD [fs ⁻¹] (from Table 14)	Shift [fs ⁻¹]
Elastic	> 10 ⁸	> 10 ⁻⁷	> 10 ⁻²	10 ⁵
Glassy	10 ⁸ –10 ⁴	10 ⁻⁷ –10 ⁻¹¹	10 ⁻² –10 ⁻⁵	10 ⁶
Rubbery	10 ⁴ –10 ⁻³	10 ⁻¹¹ –10 ⁻¹⁸	10 ⁻⁵ –10 ⁻⁸	10 ⁸
Rubbery Flow	10 ⁻³ –10 ⁻⁴	10 ⁻¹⁸ –10 ⁻¹⁹	10 ⁻⁸ –10 ⁻¹⁰	10 ⁸ –10 ⁹
Viscous Flow	< 10 ⁻⁴	< 10 ⁻¹⁹	< 10 ⁻¹⁰	10 ⁹

7. Discussion

7.1. No-shear

The molecular models, ranging from Samples 1 through 12 in Table 1, display thermophysical properties consistent with those expected and observed in compounds of similar nature and SARA fraction. As shown in Table 8, the systems exhibit densities ranging from 800 to 1100 kg/m³, heat of vaporizations of 300 kJ/kg, solubility parameters of 550 kJ^{0.5}/m^{1.5}, heat capacities of 2.2 kJ/kg, and thermal expansion coefficients of about 5.0 • 10⁻⁴ K⁻¹. These trends compare remarkably well with those reported in the literature [55,57,58,60], indicating that the molecular models, their preparation, and MD simulation setups are numerically, thermodynamically, and physically realistic.

The Saturates exhibit the lowest density and solubility parameters among all fractions, with both Samples 1 and 2 well below 950 kg/m³, while retaining the highest heat capacity. The properties of Aromatics and Resins follow, closely resembling those of conventional crude oils, with densities around 1000 kg/m³ and solubility parameters significantly higher than those of saturates. This behavior is expected, as their aromatic and polar nature enhances ability to dissolve in a wider range of hydrocarbons. The Asphaltenes have the highest densities, exceeding 1000 kg/m³ in all cases, with properties similar, but more pronounced, to those of Resins [28].

While the models are not subject to explicit external shearing de-

formations, the interactions between atoms induce instantaneous variations in both normal and shear stresses. The magnitude of the stress tensors indicates that, in all systems, the normal stresses align well with those required to exert 1 atmosphere of pressure uniformly in all directions, while the shear stresses equilibrate to maintain the simulation box's tilt factors in a quasi-orthogonal configuration (e.g., $\alpha = \beta = \gamma = 90^\circ$). This suggests an absence of numerical artifacts affecting the natural response of the systems, which can often result from molecules being unnaturally interlocked in highly energetic metastable conformations or other unnatural stress-inducing factors arising from unexpected responses to the force field parameters and the system being modeled [51]. Table 9 depicts that the surface tension of all samples averages at 0.02 N/m, which aligns well with experimental measurements of a wide array of hydrocarbons, especially crude oils [67].

The variation of σ_{xy} , denoted by the intervals shown in Table 9, is consistent and never exceeds 40 MPa across all systems. This amplitude suggests that stress measurements from subsequent simulations involving oscillatory strain rates cannot be lower than this value. This represents an intrinsic limitation of the systems modeled, the simulation setup, and the force field's capabilities to suppress or overcome numerical intricacies. This limitation is particularly detrimental when dealing with frequencies of deformation that elicit stress responses so small that they fall within the variation of no-shear stresses, complicating, if not invalidating, the interpretation of the results. While the lowest frequencies studied (10⁻⁹ fs⁻¹) still elicit moduli that are mostly above 40 MPa, it is estimated that all-atom simulations involving the samples of Table 1 and the PCFF force field begin to have difficulties in measuring external stress responses below 10⁻¹¹ fs⁻¹, as the measured stresses are expected to fall below 40 MPa. This is especially relevant when capturing stress measurements in the Rubbery and Viscous Flow regions.

The variation of σ_{xy} reaching as high as 40 MPa indicates that the stress tensors take a long time to stabilize as they vary significantly around the mean, exceeding the target stress values of approximately 0.1 MPa by two orders of magnitude. This variation is mostly attributed to instantaneous changes in intramolecular interactions, such as those introduced by the delicate balance that exists between the harmonic motion of atomic bonds and the short-range interactions of Van der Waal

forces which increase with a power of 9. These are averaged out in larger- and longer-scale simulations and experimental observations, introducing fluctuations that are not observed in realistic conditions into all-atom stress measurements. This high variation and slow stress-tensor convergence towards the desired mean is not an artifact of the simulations of this study, but rather a well-known phenomenon affecting all-atom simulations involving conventional Class II force fields [46]. Consequently, this highlights the limitations of no-shear (or low shear) approaches in computing or extracting stress-related properties, particularly for measurements below 40 MPa. The limitation does not apply to observations made using the TTS principle, which can still provide observations below the 40 MPa limitation, making its use crucial when needing near zero-shear observations.

7.2. Saturates

The Saturates fraction is characterized by having the lowest moduli of all four fractions at 25 °C, with G' , G'' , and G^* equal to 3145, 1421, and 3643 MPa, respectively. This observation remains true across all frequencies tested, as seen in Fig. 1. These values, however, are indicative of highly stiff materials, which is not common for this fraction. At this temperature, G' dominates over G'' by a factor of two, making the Saturates predominantly elastic. The corresponding viscosities, η' , η'' , and η^* are 2.14, 0.96, and 2.48 Pa s, respectively, with most of the resistance to deformation attributed to its elastic portion. Comparatively, the Saturates under these conditions are akin to soft rubber, cold honey, or liquid polyesters [68]. The unexpectedly high values, though still reasonable, can be attributed to the high degree of branching of Squalane and Hopane molecules, resulting in a higher-than-normal cross-linking activity which increases the material's stiffness [65].

The Saturates exhibit very high thermal susceptibility across all dynamic properties, with χ averaging around 0.05. At 200 °C, the values of G' , G'' , and G^* are 97, 59, and 123 MPa, respectively, the lowest among all SARA categories, indicating a substantial decrease in stiffness. The corresponding viscosities at 200 °C, η' , η'' , and η^* , are 0.067, 0.040, and 0.084 Pa s, respectively. These viscosity magnitudes compare well with those reported in the literature for engine and vegetable oils heated to similar temperatures, demonstrating how the Saturates transition from soft elastic to thin viscous within their operating conditions. Moreover, these values are consistent with studies performed on Squalane and Hopane oil, which have reported viscosity values of 0.85 and 0.5 Pa s at 25 °C and 0.01 and 0.008 Pa s at 200 °C [55].

Interestingly, simulations indicate that the storage viscosity (η') is substantially larger than the loss viscosity (η''), a phenomenon that is also observed experimentally. While the Saturates are the softest and thinnest SARA fraction, their highly branched nature, combined with the high frequency of deformation characteristic of the simulations, may impart them with a response that is somewhat more elastic when compared to other highly saturated, low molecular weight hydrocarbons.

Specifically, Hopane oil shows dynamic moduli and viscosities that average to be double those of Squalane oil at 25 °C, becoming more apparent at higher temperatures. This aligns well with experimental observations, where Hopane is roughly 2.5 to 5 times more viscous than Squalane oil, and its storage modulus can be 10 to 100 times higher than that of Squalane oil [69]. This is attributable to the polycyclic nature of Hopane molecules – in addition to their branches – resulting in greater resistance to deformation.

The dynamic properties of the Saturates fraction are very similar to those of every other fraction at very high frequencies (from 10^0 to 10^{-1} fs $^{-1}$). This occurs because the deformation rate far exceeds the fastest vibrational modes in the system (e.g., the vibrational frequency of C–H bonds) and is significantly faster than the molecules' self-diffusive behavior. Consequently, the material exhibits a purely elastic, highly stiff response, as its intrinsic dynamics lack the time to dissipate the

applied stress. This observation is expected to be consistent across all 12 samples and is therefore not exclusive to the Saturates fraction. The viscous response portion becomes significant at a frequency of 10^{-2} fs $^{-1}$, suggesting that the energy imparted into the material by rapid deformations is maximally dissipated at these frequencies. The loss modulus surpasses the storage modulus at several frequencies (10^{-3} , 10^{-5} , and 10^{-8} fs $^{-1}$), indicating multiple relaxation times in the material. It is not until the frequency falls below 10^{-8} fs $^{-1}$ that the storage modulus decreases abruptly unlike the loss modulus. This behavior suggests that, at the lower end of the tested frequency range, the Saturates fraction can exhibit a viscous flow region. This result illustrates that softer materials, such as the Saturates, display a narrower viscoelastic regime, which is captured within the frequency limits of this study.

From Table 14, the Saturates exhibit the lowest dynamic moduli and viscosities across all frequencies, especially those nearing lower frequencies. The loss viscosity stabilizes at 0.8 Pa s from 10^{-7} to 10^{-9} fs $^{-1}$. This indicates that MD simulations are realistically capturing values reported in the literature and can effectively model the very low (near zero shear) behaviors of Saturate-like compounds. Upon examining the dynamic moduli in TTS-induced frequencies (reaching microsecond-long oscillation periods) in Table 14, their magnitude continues to consistently decrease, reaching more reasonable values for mechanical moduli, now hovering around 20 MPa.

The Saturates are the only SARA fraction to exhibit characteristics of all five regions within the tested frequencies, including those reached using the TTS principle. This indicates that the range of frequencies tested successfully encompasses multiple response regimes, and that centering the frequency sweep test along the characteristic time of the material is effective and necessary. This initial finding suggests that the frequencies tested in this study capture a wide array of responses, from elastic to viscous, and highlight the need for careful scaling of MD timescales from experimental timescales. Under experimental conditions, the tested frequencies would elicit a fully elastic response, corresponding to the Elastic region, as shown in the experimentally obtained master curve for Polyisobutylene in Fig. 2.

7.3. Aromatics

The Aromatics fraction, when assessed at 25 °C, exhibits moduli values where G' , G'' , and G^* are 4554, 3239, and 5792 MPa, respectively. These values indicate that these materials are stiffer than the Saturates by a factor of 1.5. G' exceeds G'' by approximately 1.4 times, confirming a predominance of elastic behavior, although it is the smallest of all the SARA fractions. The viscosities, η' , η'' , and η^* are 3.10, 2.21, and 3.95 Pa s, respectively, illustrating a considerable resistance to deformation that leans more towards elastic recovery than viscous flow. These values are comparatively higher than those of Saturates, but considerably lower than those of Resins or Asphaltene, an observation seen in previous studies [28,56]. This behavior is comparable to thick industrial varnishes, paraffins, or heavy oils, which, while capable of flowing under prolonged stress, primarily resist deformation elastically if deformed quickly, showcasing the shear-thinning properties of bituminous materials.

At elevated temperatures of 200 °C, the Aromatics show a profound reduction in all measured properties, with G' , G'' , and G^* plummeting to 89.87, 87.02, and 147.26 MPa, respectively. This marks the highest degree of thermal softening among the SARA categories, where χ averages about 0.02 across all properties. The viscosities at this temperature, η' , η'' , and η^* , decrease to 0.061, 0.059, and 0.100 Pa s, respectively, transitioning the material behavior to closely resemble light machine oils and the Saturates fraction. This high thermal susceptibility—also observed in previous studies [55,68]—can be attributed to the reduced effectiveness of aromatic stacking due to electron delocalization of π - π interactions at elevated temperatures, leading to looser intermolecular

cohesiveness and decreased ability to resist deformation [70].

Specifically, PHPN's dynamic properties are, on average, 1.5 to 2.5 times larger than those of DOCHN, observed at both 25 °C and 200 °C. This can be attributed to PHPN's higher content of aromatic and non-aromatic rings, a more symmetric structure, and better distributed and shorter aliphatic branches, providing it with superior stacking and shorter range interlocking capabilities, thereby increasing its resistance to deformation.

The Aromatics' dynamic moduli dependency on frequency is very similar to that of the Saturates, though more stable. The loss modulus quickly overtakes the storage modulus when transitioning from very fast to slower frequencies and remains consistently dominant at slower frequencies. This observation suggests fewer relaxation times describing the behavior of the materials, possibly indicating higher stability and fewer degrees of freedom within the molecules' modes of motion compared to the branched/aliphatic nature of the Saturates.

Even though the TTS principle can cover microsecond-long oscillation periods, depicted in Table 14, most of the dynamic properties have not properly settled—possibly requiring even longer timescales to fully capture the frequency dependency of the properties down to near zero-shear domains. This can be corroborated by observing the magnitude of the dynamic moduli at 10^{-9} frequencies, which are around 30 MPa. While these values are comparatively low, they are still considerably high for Aromatics (though not unheard of), which have been reported to be as low as 0.5 MPa at near zero-shear frequencies [71].

The Aromatics also exhibit five characteristic regions, similar to the Saturates. However, Points 3 and 4 are significantly shifted towards lower frequency regions, with Point 4 nearly outside the lowest frequency estimated by the plots. This observation suggests two implications: first, the position of the elastic regions corresponding to Points 1 and 2 are less influenced by the chemical composition of the samples and frequency/temperature of the tests; second, the aromatics fraction, within the tested frequencies, shows a less viscous response, with the Rubbery region dominating the plot over a wider frequency range.

7.4. Resins

The Resins fraction is recognized for having properties that resemble those of Asphaltenes, but to a lesser extent [20]. Simulations confirm this observation, as the dynamic properties of Resins lie just below those of Asphaltenes at both 25 °C and 200 °C (clearly depicted in Fig. 1). At 25 °C, G' , G'' , and G^* are equal to 11982, 3246, and 12794 MPa, respectively, indicating that Resins are highly elastic (with G' surpassing G'' by almost four times) and very stiff, considerably more so than both Saturates or Aromatics. The corresponding viscosities, η' , η'' , and η^* , are 7.66, 1.97, and 8.17 Pa s, respectively, akin to viscosities of cold glycerin, polyisobutylene, or heavy crude oils.

Resins are affected by temperature differently than any other fraction. While their loss-related properties (G'' and η'') are very susceptible to changes in temperature, with a thermal susceptibility factor χ equal to that of Saturates at 0.05, their storage-related properties (G' and η') are much less affected, with χ sitting around 0.20. At 200 °C, G' , G'' , and G^* decrease to 309, 403, and 537 MPa, respectively, positioning them between Asphaltenes and both Saturates and Aromatics even at high temperatures.

While the Resins' response was predominantly elastic at 25 °C, at 200 °C, the situation reverses, with G'' being about 1.3 times larger than G' . This represents the largest elastic-to-viscous shift among all fractions. This change is also evident in the corresponding viscosities, which decrease to 0.21, 0.27, and 0.36 Pa s. These viscosities resemble those of kerosene and light cooking oils [68], indicating that resins could respond entirely differently within their operating conditions, both in terms of their response to deformations (e.g., elastic or viscous) and their resistance to deformation (e.g., stiff or soft).

While the Resins consist of a multitude of molecules that are often

not possible to separate or identify individually, previous studies fractionating and studying Resinous fractions as a whole report similar viscosity magnitudes (both at 25 °C and 200 °C) and a similar trend in the reversal from elastic-dominant behavior to viscous-dominant behavior [20,28]. Specifically, at 25 °C, Benzobisbenzothiophenes exhibit the highest storage modulus and storage viscosity (at 16880 MPa and 11.50 Pa s), with the highest G'/G'' ratio among all Resins. This is attributable to their small size and their highly and well-distributed aromatic and amphiphilic nature.

Conversely, Quinolinoxanes and Pyridinoxanes have the highest loss moduli and lowest viscosities among all Resins tested (approximately 2000 MPa and 1.50 Pa s), attributable to their asymmetric structure and polarities, being the least aromatic Resins of all. This trend persists at 200 °C. The significant shift in viscoelasticity can be attributed to how temperature affects the stacking potential of aromatic rings—a characteristic prevalent in Resinous molecules—being most pronounced in Benzobisbenzothiophenes. Predominantly planar regions, mainly composed of polycyclic aromatic structures, appear to play a crucial role in increasing the storage modulus of materials, especially with molecule sizes like those present in bitumen (e.g., of about 500 g/mol) [72]. Moreover, the case of some Resins is special; they are small, amphiphilic, and highly aromatic, and have been reported to crystallize rather easily into highly interlocked and packed configurations, and have been reported to do so even at warm temperatures [73]. This imparts Resins with high variability in their dynamic responses, requiring careful consideration on a compound-specific basis.

While the frequency-dependent plots of the dynamic properties of the Resins are very similar to those of other fractions at very high frequencies, the loss modulus remains consistently below the storage modulus, even at medium and low frequencies. It is only at frequencies studied using the TTS principle (very low; 10^{-7} fs $^{-1}$ and lower) that the storage modulus undergoes a significant drop, bringing it below the loss modulus. At very low frequencies, the viscosities seem to stabilize, suggesting that the frequency range tested is sufficient to study near zero-shear responses. The stabilization of the viscosities at such low frequencies can be attributed to the consistent decrease in dynamic moduli being proportional to the decrease in frequency, indicating the start of a Newtonian response regime.

The Resins exhibit four characteristic regions, with their dynamic properties shifting further to the left compared to those of the Aromatics fraction by approximately a decade. The shift becomes more pronounced at lower frequencies, widening at the regions corresponding to mostly Rubbery or Viscous responses (reaching 3 or 4 decades), while the elastic regions remain mostly unaffected and constant across all fractions, as seen in Table 1. Given that the shifting becomes more pronounced with each SARA fraction, the mass of the molecule tested seems to have a crucial impact on the frequency ranges required to characterize them. In essence, the heavier the molecule, the wider the frequency domain required to produce a response containing features of all characteristic regions.

7.5. Asphaltenes

The Asphaltenes fraction exhibits values of G' , G'' , and G^* equal to 12158, 4502, and 13200 MPa at 25 °C. These values suggest that Asphaltenes are predominantly very stiff and elastic, the most of all fractions. This is expected behavior, as Asphaltenes are known to be solid-like and very stiff at room temperature [74]. G' exceeds G'' by a factor of 3, indicating that while Asphaltenes respond less elastically than Resins, the magnitude of the shear force required to induce elastic deformations is higher than that of Resins. The viscosities at 25 °C are the highest of all fractions, slightly above those of Resins, with η' , η'' , and η^* being 8.29, 3.07, and 9.00 Pa s, respectively. While these values are not low—showcasing a viscosity akin to that of cold crude oil—Asphaltenes at room temperature have been reported to have

viscosities of hundreds, if not thousands, of pascal-seconds, as they correspond to the solid part of heavy crude oils, tars, or bitumens [75]. The exceptionally high moduli and potentially low viscosities indicate that the tested range should extend to even lower frequencies.

Asphaltenes are the least susceptible to thermal stress. When heated to 200 °C, their dynamic properties fall, on average, by a factor of 5 (with a χ factor of 0.20), resulting in G' , G'' , and G^* values of 1579, 1447, and 2183 MPa, respectively, which is akin to the Saturates fraction at 25 °C. This indicates that Asphaltenes remain stiff and/or thick even at elevated temperatures, aligning well with observations that bitumens with high Asphaltenic contents retain their structural integrity under high thermal loads [74]. Unlike Resins, the loss modulus of Asphaltenes is the least affected by thermal load, with a χ factor of only 0.32—the highest of all fractions and significantly above the average χ of 0.07 across other SARA fractions. This suggests that Asphaltenes transition from being highly stiff and elastic to viscous but considerably thick at high temperatures (both relative to other fractions and in nominal terms).

The viscosities at 200 °C, η' , η'' , and η^* , decrease to 1.07, 0.98, and 1.49 Pa s, respectively. These values are substantially higher than those of other fractions at 200 °C (most compounds' viscosities lower to about 0.01 Pa s or lower), indicating that Asphaltenes are the only fraction to resemble materials akin to industrial grease at elevated temperatures, an observation that aligns with experimental observations. These observations are consistent with experimental data, where the viscosities of Asphaltenic compounds have been reported to range from 0.5 to 100 Pa s at 160–220 °C [56,59,71].

On the frequency-dependent plots of the dynamic moduli, while Asphaltenes follow a similar trend to other fractions at very high frequencies, the loss modulus clearly crosses the storage modulus at several points (e.g., at 10^{-2} , 10^{-4} , and 10^{-9} fs $^{-1}$). This is expected, as Asphaltenes possess the most complex and pronounced chemical structures of all the fractions, indicating numerous dominant relaxation times within the same molecule. The plots' frequency range appears to be the most insufficient of all, even when considering microsecond-long oscillation times, as the dynamic moduli and viscosities do not settle at all, unlike other fractions.

Upon examining the dynamic moduli in TTS-induced frequencies in Table 14, the dynamic moduli of Asphaltenes reach magnitudes of about 800 MPa, slightly higher than those of the Resins and considerably higher than those of the Saturates or Aromatics. These observations indicate that the mechanical properties of the SARA fractions can be simplified into two groups: the Asphaltenes and Resins, which have significantly higher dynamic moduli (and correspondingly higher viscosities), and the Saturates and Aromatics, which exhibit lower dynamic moduli. This distinction becomes more pronounced as frequencies decrease or temperatures increase.

These observations, further corroborated by the high complexity of asphaltenes and the insufficiency in the frequency span range tested, suggests that all-atom MD simulations may still be insufficient to capture material responses that align well with the dynamic properties measured experimentally for Asphaltenic compounds. In experimental settings, the dynamic moduli of Asphaltenes hover around 10–100 MPa and viscosities are 2–4 orders of magnitude higher than those reported at low frequencies. This indicates that much longer oscillation time scales (from 10^{-9} to 10^{-11} – 10^{-12} fs $^{-1}$) are required to observe more characteristic regions, particularly those at near zero-shear conditions.

Asphaltenes predominantly exhibit three characteristic regions: Elastic, Glassy, and Rubbery, as shown in Table 14. The onset of the Rubbery Flow region occurs at the lowest frequency observed using the TTS principle, at 10^{-9} fs $^{-1}$. Similar observations made for the Aromatics and Resin fractions apply to the Asphaltenes. Their dynamic properties are shifted one to three decades to the left compared to the Resins, particularly in regions that are predominantly viscous. This shift imparts Asphaltenes with the most solid-like response of all fractions.

7.6. Methodology

The application of an oscillatory strain rate in the form of a sine wave is effective in producing a measurable stress response, which can be analyzed using straightforward post-processing scripts. This test is analogous to those conducted in laboratory settings, with most principles and reasoning remaining applicable. This approach offers a distinct advantage over other methods that aim to capture dynamic properties using MD, as those methods often employ simulation tests and conditions that, while simpler and faster to perform, do not align with the principles used in DMA.

The relaxation time of most samples' hovers around 10^3 fs for the Saturates and Aromatics at high temperatures, and 10^5 to 10^6 fs for the Resins and the Asphaltenes at low temperatures. Centering both the Section 4.1 and the Section 4.2 around $\tau = 100$ ps (10^4 fs) produced plots exhibiting both elastic and viscous characteristics.

7.6.1. Time scale discrepancy

An important consideration is the choice of the all-atom force field and its ability to capture stress-related phenomena within the timescales it is parameterized to function on. The PCFF is parameterized using quantum mechanical calculations and other semi-empirical approaches to match the forces of atoms and molecules [76]. While this method to generate force fields is regarded as the most suitable for capturing stress-related phenomena and is capable of accurately predicting densities, heat capacities, enthalpies of formation, and other thermodynamic properties, the complex nature of the molecules in bitumen may introduce additional modes of motion not adequately covered by the PCFF force field [29]. For example, the characteristic times required to capture the rotation of entire aliphatic branches, or the motion constraints introduced by electron delocalization effects in polycyclic aromatic regions may result in molecular conformations or motions that are not truly representative of the phenomena driving the motion of bitumen molecules, especially at longer scales.

Additionally, the PCFF is an all-atom force field that explicitly discretizes molecular systems using spheres to represent atoms only, excluding the explicit effect of lone pairs of electrons and other detailed characteristics often incorporated in more comprehensive force fields, such as the TIP4P and TIP5P 4- and 5-point water models [77]. While a less detailed particle set increases simplicity and efficiency, it imparts the molecular system with more degrees of freedom than the real system originally possesses. This increase in degrees of freedom enhances the self-diffusive potential of the particles, as the additional free space allows more extensive particle movement [9].

The increased particle motion is indeed accounted for in the parameterization and fitting of force fields to certain physical properties, ensuring, for example, that heats of vaporization match experimental values or that molecular self-diffusion behavior aligns with observed data. However, properties and phenomena outside this scope—particularly those pertinent to mechanical and rheological studies—may diverge significantly from real-world behavior.

A notable example is the calculation of molecular self-diffusion, often based on the movement of the molecule's center of mass, which may not fully capture the diffusion of individual atoms within the molecule. While this distinction might appear minor on larger scales, it can become critical when evaluating instantaneous molecular conformations that influence system dynamics, potentially affecting other physical properties.

Thus, properties that are not explicitly incorporated into the force field parameterization require careful consideration, as assumptions about their direct scalability or spatiotemporal invariance may not hold. Each property should be evaluated with this in mind, as discrepancies may arise that impact the accuracy of simulations, especially for complex behaviors not directly addressed in the force field design.

This is particularly important in non-equilibrium MD simulations,

where the dynamic properties being studied are time-dependent and rarely considered during the parameterization and design of all-atom force fields. This consideration is crucial for most phenomena relevant to studies involving bituminous mixtures, where more complex and large-scale mechanisms, such as the study of viscoelastic properties or the impact of phase separation, miscibility, and crystallization, are investigated.

This observation underscores a phenomenon previously mentioned in the paper (see Section 3.6)—how the all-atom dynamics dictated by the PCFF force field can lead to faster characteristic times, thus allowing the simulation of otherwise computationally inaccessible frequency domains (experimentally ranging from 0.1 to 100 s⁻¹, corresponding to about 10¹⁴ to 10¹⁷ simulation steps). The frequency-dependent plots reveal a wide range of characteristic regions (e.g., Elastic, Glassy, Rubbery, etc.), displaying a proper transition between elastic and viscous responses within frequency ranges that, in experimental setups, would elicit a fully elastic response.

This discrepancy suggests that, for measuring stress-related properties, particularly those influential in oscillatory tests, the timescales of the force field and real-life do not scale proportionally (1 fs⁻¹ is not equivalent to 1e-15s). This is particularly shown in Table 15, where each characteristic region has its own shift factor. There exists a point in simulations at much higher frequencies corresponding to a point in experimental tests at much lower frequencies. The shift is on average about 6 to 8 decades long, suggesting that roughly, 1 s measured in laboratory conditions corresponds to about 1 microsecond of elapsed simulation time. Therefore, placing the logarithmic mean of the frequency sweep test within the material's characteristic relaxation time in all-atom MD simulations is crucial. Moreover, aligning the relaxation times of materials over the observed timescales is a common and well-founded practice, even outside the realm of computational modeling. Studies that compare different materials and experimental set ups often adjust their characteristic times to achieve the same Deborah number, ensuring that different testing set ups produce comparable dynamic response regimes [8]. It appears that this need for alignment is equally essential when comparing simulations to experimental setups and likely extends to comparisons between computational setups as well. Even when differences are minor, simulations with slightly varied input parameters require careful adjustment of their characteristic times to ensure that the Deborah numbers are similar, thereby enabling effective comparability between the phenomena observed. This is particularly relevant in the context of NEMD, where time-dependency is pronounced, and the viscoelastic nature of the materials under study is highly sensitive to the scale of temporal variations.

One of the major limitations in simulations involving low frequencies is the selection of the time step, typically set to 1 fs for all-atom simulations. This time step is necessary for simulating frequencies slower than 10⁻⁴ s⁻¹, below which the time step cannot be proportionally increased. Consequently, simulations are fundamentally confined to an all-atom timescale space, often limited to no more than 10⁷–10⁸ steps (i.e., hundreds of nanoseconds), which is, nominally speaking, still 10⁷–10⁸ times faster than experimentally required.

Possible workarounds include using force fields designed to allow longer time steps, such as United Atom or Coarse-Grained force fields [78] using smoother potential energy hypersurfaces, those using simplifications in highly-vibratory modes of motion (e.g., by artificially fixing or disabling bonded oscillations), or others specifically parameterized for studying the dynamic properties of bituminous molecules. These force fields have been reported to achieve integration steps and equivalent times 1–4 orders of magnitude faster, capturing relaxation times within a much shorter simulation duration. However, adopting these methods would require revisiting all the spatiotemporal equivalences, hereby mentioned, with force fields known to be less conservative and transferable, introducing additional complexities [79]. Other workarounds involve the use of Accelerated MD techniques (e.g., using

higher temperatures to accelerate the motion of particles), although these would introduce more pronounced scalability discrepancies. Nonetheless, these approaches could enable the study of extremely low frequencies, reaching into the microsecond, millisecond, or even second-long range, which are currently inaccessible and incomputable using conventional all-atom simulations.

7.6.2. Other discrepancies

While there is a well-known and clear timescale discrepancy between PCFF and experimental dynamics, there also exist more implicit but equally influential considerations regarding the scalability and applicability of different strain levels in all-atom MD simulations compared to their experimental counterparts. Molecular simulations are in constant motion, regardless of the temperature tested (unless at 0 K). Given that PCFF simulations inherently have more degrees of freedom than real systems, larger strain levels are often required to produce the same mechanical response as seen in experiments. In simulations, particles experience fewer constraints on their motion, allowing stress to dissipate more readily. As a result, higher strain levels are needed to achieve comparable responses to those observed in more real materials.

Zero-shear PCFF simulations indicate that the variability of the instantaneous shear stress tensors is significant enough to prevent relevant statistical measurement of stress-related properties at very low strain levels (in the case of this study, below 1 %). This implies that there must also be some degree of equivalence accounted for when dealing with spatial-dependent properties, even if the conversion factors appear trivial at first glance (e.g., a strain of 1 % is the same across any spatial dimension). This consideration ensures that the mechanical responses observed in simulations accurately reflect those in experimental conditions, and that the stress response measured is detectable and statistically relevant.

The inherent focus of all-atom MD algorithms on replicating atomic-scale phenomena is identified as a potential source of error in estimating shear stresses, particularly during deformations. For instance, as atoms move and dissipate stress, integration algorithms adjust the velocity—thereby constraining the kinetic contribution to the Virial equation—to maintain the system's temperature. Although this temperature control effectively sustains the simulations in a thermodynamic quasi-steady state, it nullifies the impact of heat generation due to deformations, which could be more substantial in experimental observations. Future research on deformations using MD should investigate whether a less intrusive temperature control, permitting particles to temporarily reach higher temperatures, offers a more accurate representation of reality. This should be examined in conjunction with other algorithms governing particle dynamics, possibly reducing the discrepancy between the high dynamic moduli detected in this study and those obtained experimentally.

Given that frequencies, temperatures, and to some extent, strain levels can be used interchangeably, there is the concept that if spatio-temporal scale discrepancies already exist under what are considered “normal conditions” (e.g., 200 °C, TTS reaching 10⁻⁹ fs⁻¹), requiring the development of careful equivalence factors, then more extreme simulations can be conducted to explore a broader set of frequencies with the same amount of work. For example, simulations could be performed at 400 °C with TTS reaching 10⁻¹¹ fs⁻¹. However, this technique would be less conservative and would necessitate a much more careful approach when dealing with scale discrepancies, especially because such scenarios would push particles to cross potential energy barriers that are seldom, if ever, crossed under normal conditions.

7.7. Practical applications

The study of bitumen using MD has often focused on fundamental material properties, overlooking the material's primary industrial relevance. Consequently, MD applications in bituminous research have not

consistently translated into immediately applicable insights for improving, designing, customizing, or characterizing bitumen and bituminous materials. This study, while centered on the MD-based investigation of hydrocarbon mixtures, aims to bridge this gap, aligning MD insights more closely with practical needs in the construction and oil and gas industries.

This manuscript introduces a simulation framework that elucidates the mechanical and rheological responses of bituminous materials, utilizing methodologies commonly used in civil engineering and rheology. Although preliminary, this framework provides a foundation for understanding material properties beyond the basic descriptors typically obtained via MD, allowing researchers to pinpoint chemical characteristics and fundamental properties that influence material behavior with greater relevancy.

By presenting a technique for determining the dynamic properties of bituminous materials, this study encourages future research to incorporate stress-related properties into the characterization and validation of bitumen. Additionally, the introduction of characteristic times is expected to improve the transferability and comparability of computational and experimental findings, addressing a significant challenge in this field.

Furthermore, the application of MD in material studies offers substantial value by enabling the modeling, observation, and prediction of material properties without requiring experimentally defined parameters. This capability is particularly advantageous for improving the quality of machine learning techniques, which typically demand extensive data sets that are challenging to produce experimentally [80].

8. Conclusion

The application of strain-controlled oscillatory deformations in MD simulations effectively evaluates the dynamic properties of all-atom molecular systems, offering a robust method to acquire otherwise unobtainable material properties. This study models twelve molecular systems, representing all four SARA fractions of bitumen, successfully capturing their dynamic properties and differences both nominally and comparatively. The method mirrors the principles used in DMA tests, effectively distinguishing between G' and G'' , and accurately characterizing the viscoelastic responses of the samples.

The results reveal a range of moduli spanning from thousands to tens of megapascals and viscosities from tens of Pascal-seconds at lower temperatures to values akin to water at higher temperatures, aligning well with experimental observations for all SARA fractions. Saturates exhibit the softest and thinnest properties, requiring minimal energy to deform and demonstrating significant thermal susceptibility, behaving like cold honey at room temperature and hot engine oil at high temperature. Aromatics, slightly stiffer than Saturates but softer than Resins or Asphaltenes by a considerable margin, show the highest thermal susceptibility, transitioning from heavy oil-like responses at low temperatures to those of thin viscous liquids at higher temperatures. Resins, mechanically between Saturates and Asphaltenes, display the most elastic-dominant response at low temperatures, but still require less energy to deform than Asphaltenes. They undergo a significant viscoelastic change with temperature, from resembling cold heavy crude oils to light cooking oils. Asphaltenes are the stiffest and most elastic fraction, with moduli similar to tar or pitch, showing minimal thermal susceptibility and remaining thick even when heated.

While oscillatory deformation tests effectively capture material differences and compare well with experimental observations, they present several challenges. The primary limitation is the spatiotemporal scale equivalences from using parametrized, pre-computed force fields like the PCFF. This force field introduces additional degrees of freedom, particularly in bituminous molecules dominated by pi-pi interactions, accelerating system dynamics artificially. Moreover, the relaxation time in all-atom MD systems is significantly lower than experimental counterparts, necessitating stress measurements around the relaxation time

of the model and comparing these to equivalent times in another model – possibly aligning Deborah numbers between setups and materials tested to ensure similar physical response regimes.

All-atom MD simulations display accelerated dynamics, requiring fewer steps to exhibit expected mechanical response regimes. While exploring microsecond-long deformation frequencies proves insufficient for most samples, it highlights multiple characteristic regions from fully elastic to mostly viscous. Although simulations extending to 10^{11} steps might cover all characteristic regions for the samples tested, real-life observations suggest microsecond scale frequencies elicit a fully elastic response in bituminous materials.

The need for material-specific equivalence factors becomes evident when comparing MD and experimental material responses, with non-linear scaling in low-frequency regions posing significant challenges. Additionally, the PCFF force field sets intrinsic limitations on integration time steps for organic systems, affecting low-frequency characteristic regions' study due to the atomic-scale limitation of the force field. The dynamics and energy control algorithms that dictate atomic scale interactions might not align well with how energy transfers in experimental setups, influencing property measurements and increasing the discrepancies between all-atom and experimental setups. Moreover, stress tensor computations using the virial equation, dependent on instantaneous kinetic and potential energies, can lead to large short-term variations, complicating the measurement of properties under small strain levels or rates.

Despite these limitations, the method effectively captures the dynamic properties of various bituminous molecules, providing an excellent technique for studying mechanical response differences between the SARA fractions of bitumen. While the dynamic moduli are often overestimated, and their corresponding viscosities may be inaccurately represented, the measurements are consistent, follow known trends, and are closer to real observations than those obtained using other all-atom MD methods.

The findings, interpretable from rheological and civil engineering perspectives, demonstrate high similarity with laboratory rheological analyses and clearly distinguish among the SARA fractions at different frequencies and temperatures. This approach proves valuable for the mechanical evaluation and design of bituminous materials using molecular methods, offering a multidisciplinary approach to studying viscoelastic materials through computational techniques.

CRedit authorship contribution statement

Eli I. Assaf: Writing – original draft, Validation, Software, Methodology, Investigation, Formal analysis, Conceptualization. **Xueyan Liu:** Visualization, Validation, Supervision, Resources, Project administration, Funding acquisition. **Sandra Erkens:** Visualization, Validation, Supervision, Software, Resources, Project administration, Formal analysis, Conceptualization.

Declaration of competing interest

The authors declare that they have no known competing financial interests or personal relationships that could have appeared to influence the work reported in this paper.

Acknowledgements

This paper/article is created under the research program Knowledge-based Pavement Engineering (KPE). KPE is a cooperation between the Ministry of Infrastructure and Water Management (Rijkswaterstaat), TNO, and TU Delft in which scientific and applied knowledge is gained about asphalt pavements and which contributes to the aim of Rijkswaterstaat to be completely climate neutral and to work according to the circular principle by 2030. The opinions expressed in these papers are solely from the authors.

Declaration of AI and AI-assisted technologies in the writing process

During the preparation of this work the author(s) used OpenAI's ChatGPT4o to shorten the length of certain sections. After using this tool/service, the author(s) reviewed and edited the content as needed and take(s) full responsibility for the content of the publication.

Appendix A. Supplementary material

Supplementary data to this article can be found online at <https://doi.org/10.1016/j.molliq.2024.126637>.

Data availability

Most of the data necessary to showcase and discuss the contents of this paper has been provided in the [Supplementary Information](#), including the information required to replicate the majority (if not all) of the research conducted here. However, some data points have been intentionally excluded. The omission of these data points does not impact the validity of the results presented in the paper, as the available data is sufficient to support the conclusions drawn. The omitted data points are currently being utilized in an ongoing research project involving machine learning models, as they are valuable assets directly influencing the effective development of our current line of research

References

- [1] D. Lesueur, The colloidal structure of bitumen: Consequences on the rheology and on the mechanisms of bitumen modification, *Adv. Colloid Interface Sci.* 145 (1–2) (2009) 42–82.
- [2] E. Behzadfar, S.G. Hatzikiriakos, Viscoelastic properties and constitutive modelling of bitumen, *Fuel* 108 (2013) 391–399.
- [3] R.P. Chartoff, J.D. Menczel, S.H. Dillman, Dynamic mechanical analysis (DMA), in: *Thermal Analysis of Polymers: Fundamentals and Applications*, 2009, pp. 387–495.
- [4] K.P. Menard, N. Menard, *Dynamic Mechanical Analysis*, CRC Press, 2020.
- [5] G.D. Airey, A.E. Hunter, Dynamic mechanical testing of bitumen: sample preparation methods, in: *Proceedings of the Institution of Civil Engineers-Transport*, Thomas Telford Ltd, 2003, pp. 85–92.
- [6] D. Tsai, The virial theorem and stress calculation in molecular dynamics, *J. Chem. Phys.* 70 (3) (1979) 1375–1382.
- [7] L. Lin, M. Kedzzerki, Prediction of Lubricant Viscosity from Nonequilibrium Molecular Dynamics Simulation, 2021.
- [8] R. Metzler, T.F. Nonnenmacher, Fractional relaxation processes and fractional rheological models for the description of a class of viscoelastic materials, *Int. J. Plast* 19 (7) (2003) 941–959.
- [9] A.P. Lyubartsev, A. Laaksonen, On the reduction of molecular degrees of freedom in computer simulations, in: *Springer*, 2004, pp. 219–244.
- [10] O. Teleman, B. Jönsson, S. Engström, A molecular dynamics simulation of a water model with intramolecular degrees of freedom, *Mol. Phys.* 60 (1) (1987) 193–203.
- [11] A. Hopfinger, R. Pearlstein, Molecular mechanics force-field parameterization procedures, *J. Comput. Chem.* 5 (5) (1984) 486–499.
- [12] S. Piana, K. Lindorff-Larsen, D.E. Shaw, How robust are protein folding simulations with respect to force field parameterization? *Biophys. J.* 100 (9) (2011) L47–L49.
- [13] A. Franck, T. Germany, *Viscoelasticity and Dynamic Mechanical Testing*, TA Instruments, New Castle, DE, USA, 1993. AN004.
- [14] V. Vaibhav, T.W. Sirk, A. Zaccone, Timescale bridging in atomistic simulations of epoxy polymer mechanics using non-affine deformation theory, *arXiv preprint arXiv:2406.02113*, 2024.
- [15] H.J. Berendsen, Molecular dynamics simulations: the limits and beyond, in: *Computational Molecular Dynamics: Challenges, Methods, Ideas: Proceedings of the 2nd International Symposium on Algorithms for Macromolecular Modelling*, Berlin, May 21–24, 1997, Springer, 1999, pp. 3–36.
- [16] S. Cui, P. Cummings, H. Cochran, The calculation of the viscosity from the autocorrelation function using molecular and atomic stress tensors, *Mol. Phys.* 88 (6) (1996) 1657–1664.
- [17] M. Vladkov, J.-L. Barrat, Linear and nonlinear viscoelasticity of a model unentangled polymer melt: molecular dynamics and rouse modes analysis, *Macromol. Theory Simul.* 15 (3) (2006) 252–262.
- [18] Q. Liu, R. Fang, J. Wu, Viscosity calculation of bitumen system based on Debye-Stokes-Einstein (DSE) theory using an improved averaging strategy, *Fuel* 372 (2024) 132129.
- [19] G. Raos, M. Moreno, S. Elli, Computational experiments on filled rubber viscoelasticity: what is the role of particle-particle interactions? *Macromolecules* 39 (19) (2006) 6744–6751.
- [20] D.D. Li, M.L. Greenfield, Viscosity, relaxation time, and dynamics within a model asphalt of larger molecules, *J. Chem. Phys.* 140 (3) (2014).
- [21] F. Müller-Plathe, A simple nonequilibrium molecular dynamics method for calculating the thermal conductivity, *J. Chem. Phys.* 106 (14) (1997) 6082–6085.
- [22] L. Zhao, X. Wang, L. Wang, H. Sun, Prediction of shear viscosities using periodic perturbation method and OPLS force field, *Fluid Phase Equilib.* 260 (2) (2007) 212–217.
- [23] B. Hess, Determining the shear viscosity of model liquids from molecular dynamics simulations, *J. Chem. Phys.* 116 (1) (2002) 209–217.
- [24] Z. Chen, J. Pei, R. Li, F. Xiao, Performance characteristics of asphalt materials based on molecular dynamics simulation—a review, *Constr. Build. Mater.* 189 (2018) 695–710.
- [25] S. Ren, X. Liu, P. Lin, S. Erkens, Y. Xiao, Chemo-physical characterization and molecular dynamics simulation of long-term aging behaviors of bitumen, *Constr. Build. Mater.* 302 (2021) 124437.
- [26] L.W. Corbett, Composition of asphalt based on generic fractionation, using solvent deasphalting, elution-adsorption chromatography, and densimetric characterization, *Anal. Chem.* 41 (4) (1969) 576–579.
- [27] R. Saal, J. Labout, Rheological properties of asphaltic bitumen, *J. Phys. Chem.* 44 (2) (1940) 149–165.
- [28] S. Ashoori, M. Sharifi, M. Masoumi, M. Mohammad Salehi, The relationship between SARA fractions and crude oil stability, *Egypt. J. Pet.* 26 (1) (2017) 209–213.
- [29] H. Sun, S.J. Mumby, J.R. Maple, A.T. Hagler, An ab initio CFF93 all-atom force field for polycarbonates, *J. Am. Chem. Soc.* 116 (7) (1994) 2978–2987.
- [30] M. Deserno, C. Holm, How to mesh up Ewald sums. II. An accurate error estimate for the particle-particle-particle-mesh algorithm, *J. Chem. Phys.* 109 (18) (1998) 7694–7701.
- [31] H. Sun, Z. Jin, C. Yang, R.L. Akkermans, S.H. Robertson, N.A. Spensley, S. Miller, S. M. Todd, COMPASS II: extended coverage for polymer and drug-like molecule databases, *J. Mol. Model.* 22 (2016) 1–10.
- [32] B.R. Brooks, C.L. Brooks III, A.D. Mackerell Jr, L. Nilsson, R.J. Petrella, B. Roux, Y. Won, G. Archontis, C. Bartels, S. Boresch, CHARMM: the biomolecular simulation program, *J. Comput. Chem.* 30 (10) (2009) 1545–1614.
- [33] J. Wang, R.M. Wolf, J.W. Caldwell, P.A. Kollman, D.A. Case, Development and testing of a general amber force field, *J. Comput. Chem.* 25 (9) (2004) 1157–1174.
- [34] G. Landrum, Rdkit documentation, Release 1 (1–79) (2013) 4.
- [35] T.A. Halgren, Merck molecular force field. I. Basis, form, scope, parameterization, and performance of MMFF94, *J. Comput. Chem.* 17 (5–6) (1996) 490–519.
- [36] M.C. Payne, M.P. Teter, D.C. Allan, T. Arias, A.J. Joannopoulos, Iterative minimization techniques for ab initio total-energy calculations: molecular dynamics and conjugate gradients, *Rev. Mod. Phys.* 64 (4) (1992) 1045.
- [37] F. Godey, M.O. Bensaid, A. Soldera, Extent of the glass transition in polymers envisioned by computation of mechanical properties, *Polymer* 164 (2019) 33–38.
- [38] N.A. Zarkevich, H. Chen, V.I. Levitas, D.D. Johnson, Deformation, lattice instability, and metallization during solid-solid structural transformations under general applied stress tensor: example of Si I-> Si II, *arXiv preprint arXiv:1806.00055*, 2018.
- [39] E.I. Assaf, X. Liu, P. Lin, S. Erkens, SMI2PDB: A self-contained Python tool to generate atomistic systems of organic molecules using their SMILES notations, *Software Impacts* (2024) 100655.
- [40] E.I. Assaf, X. Liu, P. Lin, S. Erkens, PDB2DAT: Automating LAMMPS data file generation from PDB molecular systems using Python, Rdkit, and Pysimm, *Software Impacts* (2024) 100656.
- [41] D.J. Evans, B.L. Holian, The nose–hoover thermostat, *J. Chem. Phys.* 83 (8) (1985) 4069–4074.
- [42] S. Ebrahimi, M. Meunier, A. Soldera, Molecular dynamics simulation of the dynamical mechanical analysis of polybutadiene, *Polym. Test.* 111 (2022) 107585.
- [43] J.P. Ewen, H.A. Spikes, D. Dini, Contributions of molecular dynamics simulations to elastohydrodynamic lubrication, *Tribol. Lett.* 69 (1) (2021) 24.
- [44] J. Padding, W.J. Briels, Zero-shear stress relaxation and long time dynamics of a linear polyethylene melt: a test of Rouse theory, *J. Chem. Phys.* 114 (19) (2001) 8685–8693.
- [45] R. Esmaeili, H. Aliniagerdroudbari, S.R. Hashemi, S. Farhad, Designing a new dynamic mechanical analysis (DMA) system for testing viscoelastic materials at high frequencies, *Modell. Simul. Eng.* 2019 (1) (2019) 7026267.
- [46] A.P. Thompson, S.J. Plimpton, W. Mattson, General formulation of pressure and stress tensor for arbitrary many-body interaction potentials under periodic boundary conditions, *J. Chem. Phys.* 131 (15) (2009).
- [47] J.D. Ferry, *Viscoelastic Properties of Polymers*, John Wiley & Sons, 1980.
- [48] A.Y. Kuksin, I. Morozov, G. Norman, V. Stegailov, I. Valuev, Standards for molecular dynamics modelling and simulation of relaxation, *Mol. Simul.* 31 (14–15) (2005) 1005–1017.
- [49] S. Abbott, *The abbott guide to rheology*, 2018, Available www.steve.nabbott.co.uk.
- [50] T. Dotson, *Relaxation Behavior in Molecular Dynamics Simulations of Simple Polymers*, Citeseer, 2008.
- [51] M. Hummel, W. Verestek, S. Schmauder, *Molecular Dynamics Simulations—A Time and Length Scale Investigation*, High Performance Computing in Science and Engineering '19: Transactions of the High Performance Computing Center, Stuttgart (HLRS), 2019, Springer, 2021, pp. 125–141.
- [52] P.M. Singer, D. Asthagiri, W.G. Chapman, G.J. Hirasaki, Molecular dynamics simulations of NMR relaxation and diffusion of bulk hydrocarbons and water, *J. Magn. Reson.* 277 (2017) 15–24.
- [53] P.J. Daivis, B. Todd, A simple, direct derivation and proof of the validity of the SLLOD equations of motion for generalized homogeneous flows, *J. Chem. Phys.* 124 (19) (2006).
- [54] J.P. Ewen, E.R. Fernández, E.R. Smith, D. Dini, Nonequilibrium molecular dynamics simulations of tribological systems, in: M. Paggi, D. Hills (Eds.), *Modeling and Simulation of Tribological Problems in Technology*, Springer International Publishing, Cham, 2020, pp. 95–130.

- [55] O. Fasina, Z. Colley, Viscosity and specific heat of vegetable oils as a function of temperature: 35 C to 180 C, *Int. J. Food Prop.* 11 (4) (2008) 738–746.
- [56] B. Hofko, L. Eberhardsteiner, J. Füssl, H. Grothe, F. Handle, M. Hospodka, D. Grossegger, S. Nahar, A. Schmets, A. Scarpas, Impact of maltene and asphaltene fraction on mechanical behavior and microstructure of bitumen, *Mater. Struct.* 49 (2016) 829–841.
- [57] W. Fang, Q. Lei, R. Lin, Enthalpies of vaporization of petroleum fractions from vapor pressure measurements and their correlation along with pure hydrocarbons, *Fluid Phase Equilib.* 205 (1) (2003) 149–161.
- [58] N. Durupt, A. Aoulmi, M. Bouroukba, M. Rogalski, Heat capacities of liquid polycyclic aromatic hydrocarbons, *Thermochim. Acta* 260 (1995) 87–94.
- [59] R. Cassis, N. Fuller, L.G. Hepler, R.J. McLean, A. Skauge, Specific Heat Capacities of Bitumens in Heavy Oils, Reservoir Minerals, Clays, Dehydrated Clays, Asphaltenes, and Cokes.
- [60] A.C.S. Ramos, M.P. Rolemberg, L.G.M. Moura, E.L. Zilio, M.F.P. Santos, G. González, Determination of solubility parameters of oils and prediction of oil compatibility, *J. Pet. Sci. Eng.* 102 (2013) 36–40.
- [61] H.W. Bearce, E.L. Peffer, Density and Thermal Expansion of American Petroleum Oils, US Government Printing Office, 1916.
- [62] B. Herzog, D. Gardner, R. Lopez-Anido, B. Goodell, Glass-transition temperature based on dynamic mechanical thermal analysis techniques as an indicator of the adhesive performance of vinyl ester resin, *J. Appl. Polym. Sci.* 97 (2005) 2221–2229.
- [63] C.A. Mahieux, Effect of temperature on polymer matrix composites, in: *Environmental Degradation of Industrial Composites*, Elsevier, Amsterdam, The Netherlands, 2006, pp. 17–83.
- [64] M. Ohring, *Engineering Materials Science*, Academic Press, 1995.
- [65] H.F. Brinson, L.C. Brinson, Polymer engineering science and viscoelasticity, *An Introduction* 99 (2008) 157.
- [66] E. Catsiff, A. Tobolsky, Stress-relaxation of polyisobutylene in the transition region (1, 2), *J. Colloid Sci.* 10 (4) (1955) 375–392.
- [67] C.L. Yaws, P.C. Richmond, Surface tension—organic compounds, in: *Thermophysical Properties of Chemicals and Hydrocarbons*, Elsevier, 2009, pp. 686–781.
- [68] D.S. Viswanath, T.K. Ghosh, D.H. Prasad, N.V. Dutt, K.Y. Rani, *Viscosity of Liquids: Theory, Estimation, Experiment, and Data*, Springer Science & Business Media, 2007.
- [69] K.A. Schmidt, D. Pagnutti, M.D. Curran, A. Singh, J.M. Trusler, G.C. Maitland, M. McBride-Wright, New experimental data and reference models for the viscosity and density of squalane, *J. Chem. Eng. Data* 60 (1) (2015) 137–150.
- [70] C.A. Hunter, J.K. Sanders, The nature of pi-pi interactions, *J. Am. Chem. Soc.* 112 (14) (1990) 5525–5534.
- [71] S. Al-Obaidi, Investigation of rheological properties of heavy oil deposits, in: *Conference of the Arabian Journal of Geosciences*, Springer, 2019, pp. 399–402.
- [72] H. Brandt, E. Hendriks, M. Michels, F. Visser, Thermodynamic modeling of asphaltene stacking, *J. Phys. Chem.* 99 (26) (1995) 10430–10432.
- [73] L.-L. Zhang, G.-H. Yang, J.-Q. Wang, Y. Li, L. Li, C.-H. Yang, Study on the polarity, solubility, and stacking characteristics of asphaltenes, *Fuel* 128 (2014) 366–372.
- [74] L. Eberhardsteiner, J. Füssl, B. Hofko, F. Handle, M. Hospodka, R. Blab, H. Grothe, Influence of asphaltene content on mechanical bitumen behavior: experimental investigation and micromechanical modeling, *Mater. Struct.* 48 (2015) 3099–3112.
- [75] K.S. Pedersen, A. Fredenslund, P.L. Christensen, P. Thomassen, Viscosity of crude oils, *Chem. Eng. Sci.* 39 (6) (1984) 1011–1016.
- [76] H. Heinz, T.-J. Lin, R. Kishore Mishra, F.S. Emami, Thermodynamically consistent force fields for the assembly of inorganic, organic, and biological nanostructures: the INTERFACE force field, *Langmuir* 29 (6) (2013) 1754–1765.
- [77] T.J. Dick, J.D. Madura, A review of the TIP4p, TIP4p-ew, TIP5p, and TIP5p-e water models, *Ann. Rep. Comput. Chem.* 1 (2005) 59–74.
- [78] E.I. Assaf, X. Liu, P. Lin, S. Erkens, Introducing a force-matched united atom force field to explore larger spatiotemporal domains in molecular dynamics simulations of bitumen, *Mater. Des.* 240 (2024) 112831.
- [79] D.-D. Jiang, J.-L. Shao, Equivalence analysis between Quasi-coarse-grained and Atomistic Simulations, *arXiv preprint arXiv:2405.05070*, 2024.
- [80] E.I. Assaf, X. Liu, P. Lin, S. Ren, S. Erkens, Predicting the properties of bitumen using machine learning models trained with force field atom types and molecular dynamics simulations, *Mater. Des.* 246 (2024) 113327.